Geological Society of America Bulletin, published online on 21 January 2011 as doi:10.1130/B30150.1

Geologic versus geodetic deformation adjacent to the San Andreas fault, central California

Sarah J. Titus[1,†], Mark Dyson[1], Charles DeMets[2], Basil Tikoff[2], Frederique Rolandone[3], and Roland Bürgmann[4]
[1]*Department of Geology, Carleton College, 1 N. College St., Northfield, Minnesota 55057, USA*
[2]*Department of Geoscience, University of Wisconsin, 1215 W. Dayton St., Madison, Wisconsin 53706, USA*
[3]*Institut des Sciences de la Terre Paris, UMR 7193UPMC-CNRS, Université Pierre et Marie Curie, 4 place Jussieu, F-75005, Paris, France*
[4]*Department of Earth and Planetary Science, University of California, 307 McCone Hall, Berkeley, California 94720, USA*

ABSTRACT

We combine geologic and global positioning system (GPS) data to characterize the style and magnitude of off-fault deformation across the San Andreas fault system in central California. Geologic structures record ~12 km of both fault-parallel and fault-perpendicular displacements across creeping and locked portions of the San Andreas fault. Analysis of 150 GPS site velocities suggests that the borderlands record 4–6 mm/yr of fault-parallel and 3–5 mm/yr of fault-perpendicular motion alongside the creeping segment, where elastic strain is minimized. The distribution of both long-term geologic and short-term geodetic deformation is affected by basement type, where more deformation is concentrated northeast of the San Andreas fault on Franciscan basement. We suggest that at least half the fault-parallel GPS deformation measured by GPS bordering the creeping segment must be accommodated by geologic structures; this permanent deformation needs to be incorporated into dynamic models of the fault system.

Elastic modeling of the San Andreas fault in central California, which incorporates its well-known transition from locked to creeping behavior near Parkfield, predicts first-order variations in the GPS velocity field along the fault and corresponding variations in dilatational strain rates. The strain rate pattern is dominated by a large contractional region northeast of the transition from locked to creeping behavior and a large extensional region southwest of the transition. The former coincides with the Coalinga and Kettleman Hills anticlines, the growth and development of which seem to have occurred under at least two kinematic conditions. We suggest that the onset of fault creep in central California promoted the growth of these folds. By implication, fault creep has been active over geologic time scales.

INTRODUCTION

To fully assess deformation and seismic hazards in active strike-slip fault systems, the relative contributions of discrete slip on major faults and distributed deformation in the fault borderlands must be quantified. Geologic measurements can be used to estimate both components, independent of one another, although these estimates are often imprecise due to uncertainties in the ages of rocks as well as the timing and magnitude of deformation. In contrast, modern geodetic measurements provide well-defined, precise measurements of active deformation that simultaneously record long-term fault slip rates, distributed deformation in the fault borderlands, elastic strain due to interseismic fault locking, and time-dependent effects related to the earthquake cycle (Savage and Prescott, 1978). Because the latter two effects can mimic long-term distributed deformation, separating the discrete and distributed components of short-term geodetic deformation is challenging. A simplifying approach frequently used to model geodetic velocities in strike-slip fault systems is to embed one or more faults in an elastic half-space and adjust the long-term fault slip rates and magnitude and distribution of frictional locking along those faults to match the geodetic velocity gradients (Savage and Burford, 1970). Because such fault-centric models exclude permanent off-fault deformation (such as folding and deformation by small secondary faults), they overestimate the role that the primary faults play in accommodating motion across deforming systems and underestimate the role of permanent deformation in the fault borderlands.

The creeping segment of the San Andreas fault is perhaps the best place for separating permanent and elastic deformation in the borderlands of a strike-slip fault. Decades of geodetic measurements along the central creeping segment have yielded steady or nearly steady fault creep rates of 28–30 mm/yr (Burford and Harsh, 1980; Lisowski and Prescott, 1981; Schulz, 1989; Titus et al., 2006), consistent within uncertainties in Holocene geologic slip rates (Sieh and Jahns, 1984; Cotton et al., 1986). The consistency of the short-term and Holocene slip rates coupled with an absence of large-magnitude earthquakes along this segment of the fault suggests that elastic strain due to interseismic locking of the fault is small or possibly zero and may thus contribute little or nothing to the off-fault velocity gradient.

Because elastic strain is minimized along the creeping segment, we have the rare opportunity to directly compare and contrast estimates of long-term deformation from the geologic record with short-term deformation from the global positioning system (GPS) velocity field from the borderlands of a major strike-slip fault. We first present our geologic analysis of off-fault deformation, which includes both a map-based approach and the summation of cumulative displacements across the fault system. Regional GPS data are then presented in these same two frameworks—map view and as velocity gradients—and the GPS velocity field is used to derive strain rate and dilatation rates for off-fault regions. Forward elastic modeling of the velocity field is used to investigate how the change from locked to creeping behavior along the San Andreas fault influences patterns of short-term, off-fault deformation.

We conclude by integrating the long-term and short-term data sets to achieve a fuller understanding of deformation in the borderlands. Because our geologic results demonstrate that the fault-parallel component of permanent deformation is as large as the fault-perpendicular component, we suggest that previous elastic

[†]E-mail: stitus@carleton.edu

 doi: 10.1130/B30150.1; 14 figures; 1 table; Data Repository item 2011010.

Geological Society of America Bulletin, published online on 21 January 2011 as doi:10.1130/B30150.1

models have overestimated the long-term slip rate on the San Andreas fault in central California by as much as ~3 mm/yr. Because the geodetic analysis demonstrates the importance of the transition from creeping to locked behavior on the San Andreas fault, we reinterpret local enigmatic geologic structures, including the Coalinga and Kettleman Hills anticlines, the histories of which are incompatible with a single set of kinematic conditions. Instead, we propose that fault creep has been active for at least 2–2.5 m.y. in central California and is reflected in the development of particular geologic structures near the transition zone.

GEOLOGIC SETTING

The San Andreas fault system was initiated in central California after passage of the Mendocino triple junction, which occurred at ca. 15 Ma (e.g., Atwater, 1970; Dickinson, 1997). The relative plate motion across this boundary eventually changed from oblique divergence, responsible for local basin formation along the California margin (Blake et al., 1978), to oblique convergence, resulting in transpression and uplift of western California (e.g., Montgomery, 1993). Although this change in kinematics is widely agreed upon, estimates of the timing of transpression vary. Some studies suggest onset at 3.2 Ma to 5 Ma (Cox and Engebretson, 1985; Pollitz, 1986; Harbert, 1991), consistent with uplift in the Coast Ranges from geologic evidence (Christensen, 1965; Page et al., 1998), whereas more recent global plate motion circuits (Atwater and Stock, 1998) set the onset of transpression at 8 Ma, consistent with uplift rates (Ducea et al., 2003) and the time necessary for the development of topographic relief in the Coast Ranges (Argus and Gordon, 2001).

In central California, plate boundary motion is accommodated on numerous structures across a 200-km-wide region (Fig. 1). These structures include the three major, subparallel, strike-slip faults—the San Gregorio–Hosgri, Rinconada, and San Andreas faults—and the borderlands between these faults. Our analysis is focused on quantifying deformation across a large portion of this region, between the Nacimiento fault and the western edge of the Great Valley. This portion of the plate boundary region was chosen because of data availability for both long-term and short-term analyses. Basement rocks in this area are typically Mesozoic in age (e.g., Ernst, 1981). Northeast of the San Andreas fault, basement rocks include the graywacke, shale, mafic volcanic rocks, limestones, and metamorphic rocks of the Franciscan complex as well as marine sedimentary rocks of the Great Valley sequence. The Franciscan complex is interpreted as accreted subduction-related material and includes ophiolite and serpentine fragments, such as the New Idria body. The Great Valley sequence is composed of marine sediments deposited in a forearc basin (Dickinson and Rich, 1972) and is interpreted to rest on the Coast Range ophiolite (e.g., Godfrey et al., 1997). West of the San Andreas fault and east of the Nacimiento fault, Cretaceous-age granites and metamorphic rocks make up the Salinian block, an allochthonous arc terrane that originated from the southern end of the Sierra Nevada batholith (Hill and Dibblee, 1953; Page, 1981). Tertiary and Quaternary sediments are deposited on top of basement rocks across the region.

Next, we summarize what is known about the major regional faults, including their discrete offsets and estimated slip rates, as well as the types of geologic structures developed in the borderlands flanking the faults.

Fault Offsets

The San Gregorio–Hosgri fault has been active since the mid-Miocene (Clark, 1998) and presently runs offshore for much of its extent. Recent work suggests a total of 156 ± 4 km of right-lateral displacement along the fault (Dickinson et al., 2005) with geologically estimated slip rates of 1–7 mm/yr (Simpson et al., 1997). The present slip rate is estimated at 3 ± 2 mm/yr (WGCEP, 2002; Hanson et al., 2004; Bird, 2009), but based on the total Neogene offset, slip rates must have been higher in the past (Dickinson et al., 2005).

The Rinconada fault has been active since the early Tertiary, with 44 ± 4 km of offset during the Neogene (Graham, 1976) and 18 km for Pliocene-age formations (Dibblee, 1976). Although no offsets of Holocene-age units have been documented (Dibblee, 1976), the current slip rate is estimated at 1–2 mm/yr (Bilham and Bodin, 1992).

The San Andreas fault has well-defined piercing points from Miocene volcanic rocks (Matthews, 1976; Sims, 1993) and Miocene shoreline assemblages (Ross, 1970; Nilsen, 1984) suggesting a net displacement of 315 ± 10 km (Graham et al., 1989). In central California, the fault is presently characterized by aseismic creep between San Juan Bautista and Cholame (Fig. 1; Allen, 1968; Burford and Harsh, 1980). Due to changing creep rates along the fault, the creeping segment is divided into northwest, central, and southeast segments (Burford and Harsh, 1980). Maximum creep rates of 28–30 mm/yr occur along the central segment between Bitterwater and Slack Canyon, based on creep meters (Schulz et al., 1982; Schulz, 1989), theodolite surveys of alignment arrays (Burford and Harsh, 1980), trilateration networks (Lisowski and Prescott, 1981), continuous and differential GPS data (Titus et al., 2005, 2006), and InSAR (Interferometric synthetic aperture radar) (Ryder and Bürgmann, 2008). No major earthquakes have occurred along the central creeping segment in the last century, although historical earthquakes in the 1850s to 1880s may have ruptured this segment of the fault (Toppozada et al., 2002, 2006). Along the northwest (or San Juan Bautista) segment, creep rates decrease to zero toward the locked section of the fault northwest of San Juan Bautista (Johanson and Burgmann, 2005), which last ruptured in the 1906 San Francisco earthquake. Similarly, creep rates decrease to zero along the southeast (or Parkfield) segment between Slack Canyon and Cholame; the locked segment southeast of Cholame last ruptured in the 1857 Fort Tejon earthquake.

Both the northwest and southeast segments are characterized by combined aseismic creep and moderate earthquakes, most recently the 1998 M5.3 San Juan Bautista and 2004 M6.0 Parkfield earthquakes (Fig. 1). Along these transition segments, creep rates can be variable, changing in response to earthquakes along the San Andreas fault (King et al., 1977; Mavko, 1982; Burford, 1988; Gladwin et al., 1994) or due to regional earthquakes, such as the 1983 Coalinga earthquake (Mavko et al., 1985; Simpson et al., 1988). In contrast, the creep rate along the central segment appears to be constant, at least for the past 35 yr (Titus et al., 2005), and perhaps up to the past century (Cashman et al., 2007), and showed no evidence for changing creep rates following the 2004 Parkfield earthquake (Titus et al., 2006).

While there are other faults throughout central California (Fig. 1), displacements on these faults are less well documented. For example, the Nacimiento fault, which is an important boundary between Salinian and Franciscan basement (Page, 1970), has an enigmatic kinematic history with possible sinistral motion during the Cretaceous (Dickinson, 1983). Offset and slip rates on other faults, such as the Waltham Canyon thrust fault, which parallels the San Andreas fault in central California (Fig. 1B), and blind faults coring folds such as the Coalinga anticline, are poorly constrained.

Borderland Deformation

The Rinconada fault passes through the Salinian block and has a well-developed fold-and-thrust belt exposed in Cretaceous through Pliocene-age sedimentary rocks within ~15 km of the fault. Folds immediately adjacent to the fault are typically within Miocene-age rocks;

Geological Society of America Bulletin, published online on 21 January 2011 as doi:10.1130/B30150.1

these are flanked to the west by folds within Mesozoic-age rocks and to the east by folds within Pliocene- and Quaternary-age rocks (Fig. 2). Fold hinges are typically en echelon and oblique to the fault strike, and their orientations vary across the region (Dibblee, 1976). These orientation changes seem to be more strongly related to position relative to the Rinconada fault rather than the age of folded rocks. Salinian granites are occasionally exposed west of the fold-and-thrust belt, with foliations and folded internal markers (e.g., quartz diorite dikes) subparallel to the fault (Compton, 1966).

Little deformation is observed between the fold-and-thrust belt flanking the Rinconada fault and the San Andreas fault to the east (Fig. 2). The Salinas Valley shows no evidence of surficial deformation; an early gravity survey found an ~30 mGal negative gravity anomaly over the valley, indicating that the depth to bedrock increases in this area (Byerly, 1966). The rocks in the Gabilan Range adjacent to the San Andreas fault are flat-lying Tertiary sedimentary rocks, and Salinian basement is closer to the surface than in the Salinas Valley, with basement granites occasionally exposed throughout the area. The only region with evidence for significant deformation is a 5–10-km-wide band immediately southwest of the San Andreas fault where en echelon folds with steep-to-overturned limbs are present in Pliocene and younger rocks (Dibblee, 1971).

Northeast of the San Andreas fault, numerous folds have developed on Franciscan basement, although the style of deformation varies with distance from the fault (Fig. 2). Within ~15 km of the fault, Cretaceous- through Pliocene-age rocks are folded with short en echelon hinges oblique to the fault strike. This folded region is bounded on the northeast by the Waltham Canyon thrust fault, which parallels the San Andreas for much of its length (Fig. 1B). From 15 km to 30 km from the fault, larger structures have developed, including the Vallecitos syncline (Fig. 2), a 40-km-long, asymmetric fold with a steep-to-overturned southern limb and more shallowly dipping northern limb (Enos, 1961). Nearby, the New Idria serpentine body is exposed in the core of another large fold that parallels the Vallecitos syncline, interpreted as either the northwest continuation of the Coalinga anticline (Tsujimori et al., 2007) or the Joaquin Ridge anticline (Wentworth and Zoback, 1989). These large folds, with 25–50-km-long hinges, are ~30° oblique to the San Andreas fault and often contain older Tertiary and Cretaceous sedimentary rocks. Beyond ~30 km northeast of the San Andreas fault, the basic style of deformation changes to long fault-parallel folds, such as the Coalinga and Kettleman Hills anticlines,

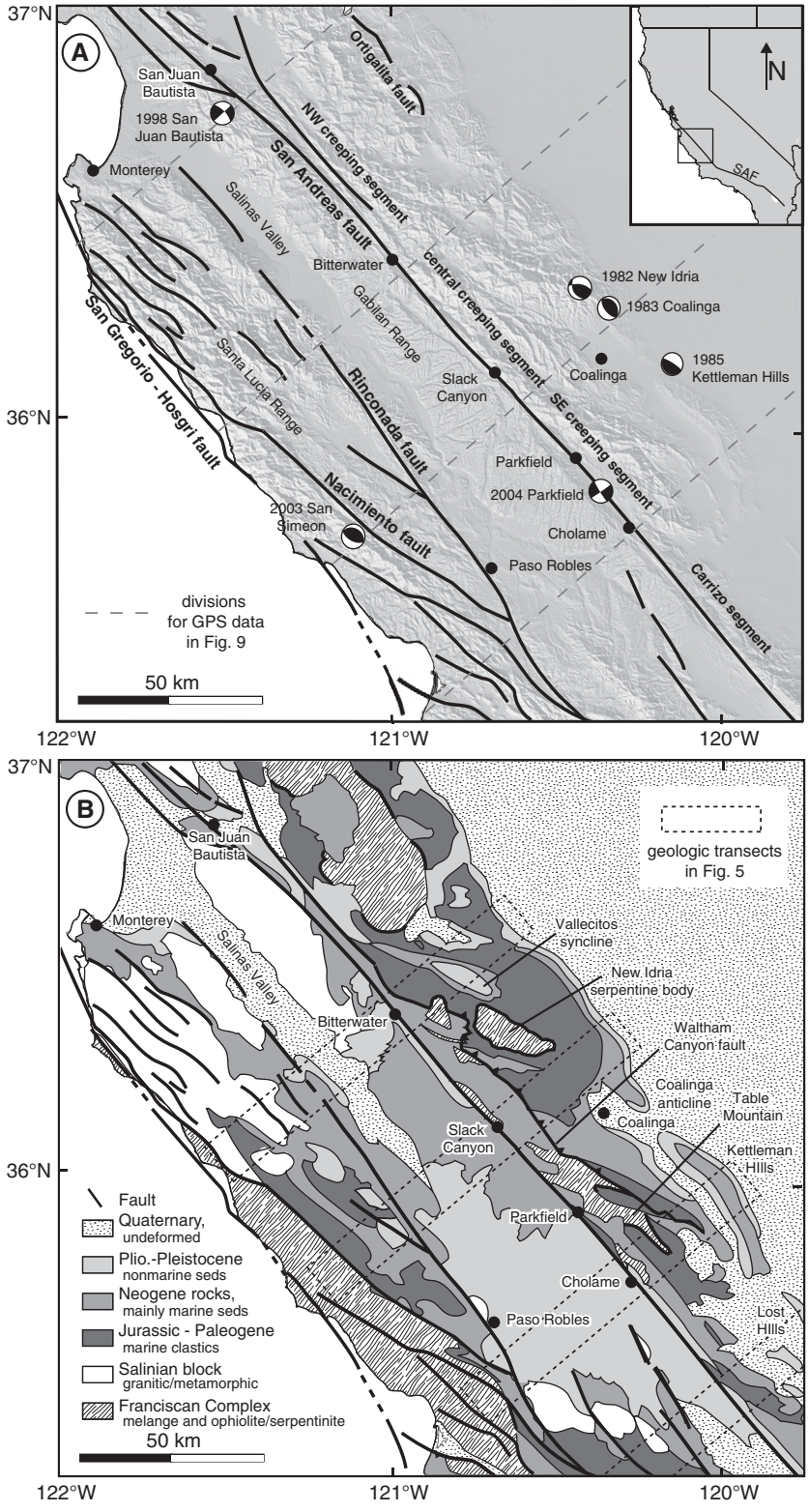

Figure 1. (A) Digital elevation map and (B) geologic map of central California modified from Jennings et al. (1977) and Page et al. (1998). Place names and major geologic features mentioned in the text are included on these maps. Divisions used for our geodetic analysis in Figure 9 are indicated by the dashed lines in A, which correspond to the northwest, central, and southeast segments of the creeping segment. Our geologic transects in Figure 5 are indicated by the dashed boxes in B.

Geological Society of America Bulletin, published online on 21 January 2011 as doi:10.1130/B30150.1

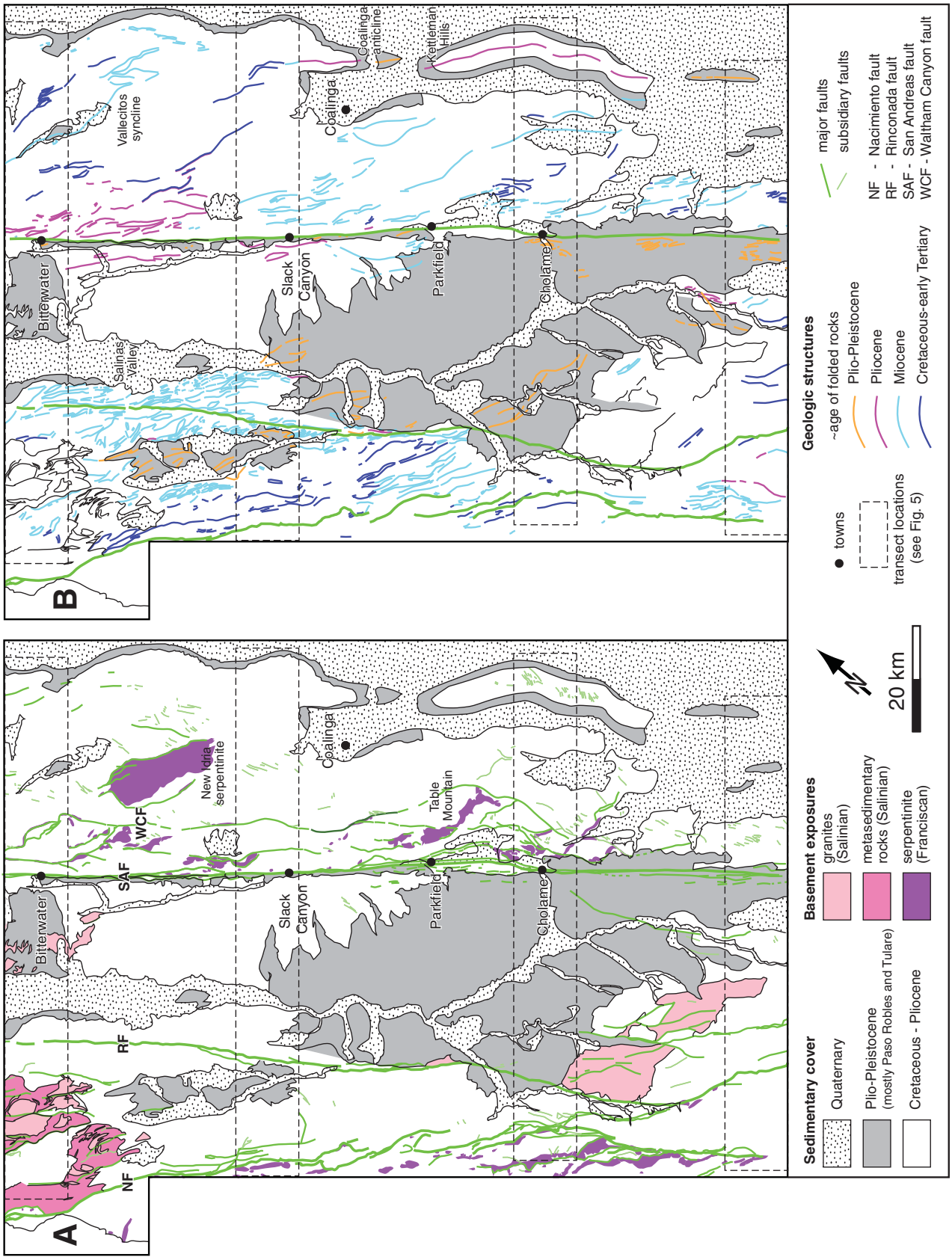

Figure 2. Detailed geologic maps of central California showing (A) faults with surficial exposures of Salinian granites and metasedimentary rocks (southwest of the San Andreas fault) and Franciscan serpentinites (northeast of the San Andreas fault and southwest of the Nacimiento fault); and (B) fold hinge orientations divided by approximate age of folded rocks. Data were compiled from mapping by Dibblee, including U.S. Geological Survey Open-File reports (1971, 1972), Dibblee Foundation maps (numbers 206, 210, 211, 215, 363, 365, 368), and the map of the Carrizo segment by Dibblee et al. (1999).

Geological Society of America Bulletin, published online on 21 January 2011 as doi:10.1130/B30150.1

the folded forms of which are often expressed in the topography (Fig. 2). These folds typically involve Pliocene- to Pleistocene-age rocks, suggesting that they are relatively recent features. These younger folds are interpreted to be cored by blind thrust faults (e.g., Wentworth and Zoback, 1989) and were the locus of three southeastward-propagating earthquakes and their aftershocks in the 1980s (Fig. 1; Ekström et al., 1992; Stein and Ekström, 1992).

LONG-TERM DEFORMATION FROM GEOLOGIC DATA

We use two complementary strategies to characterize patterns of long-term deformation in the borderlands adjacent to the Rinconada and San Andreas faults. To examine broad but somewhat qualitative spatial patterns of deformation throughout central California, we use data from folds as input in a transpressional kinematic model. To quantify the magnitude of deformation recorded between the Great Valley and the Nacimiento fault, we sum the fault-parallel and fault-perpendicular displacements recorded by geologic structures along several transects.

Map Analysis of Folding

Kinematic models for folding typically assume a particular geometry for the fold shape, which influences quantitative interpretations about folding. Classic examples include models for fault-bend folds (Suppe, 1985), fault-propagation folds (Chester and Chester, 1990; Suppe and Medwedeff, 1990), trishear geometries (Erslev, 1991; Allmendinger, 1998), or detachment folds (Jamison, 1987; Dahlstrom, 1990; Mitra, 2002, 2003). These models typically characterize deformation in cross section alone, thereby assuming that no material leaves the plane of the cross section. For the fold-and-thrust belts in the borderlands in central California, this assumption prohibits models from characterizing any fault-parallel deformation, despite field evidence to the contrary, including the en echelon arrangement of fold hinges (Miller, 1998) and paleomagnetic data supporting vertical-axis rotations in the borderlands (White, 1987; Tetreault, 2006; Titus et al., 2007).

Instead of characterizing fold geometries in cross section, we examine their characteristics in map view to estimate the San Andreas fault-parallel and fault-perpendicular components of deformation. Our data come from fold hinge orientations and limb dips available on regional geologic maps. We analyze these data using a mathematical (as opposed to geometrical) kinematic model of transpression, which is appropriate for deformation in central California given the slight obliquity between the relative plate motion and the strike of the San Andreas fault.

Transpressional Kinematic Model

While several types of transpressional kinematic models are commonly applied to geologic problems (e.g., Sanderson and Marchini, 1984; Lin et al., 1998; Jones et al., 2004), we choose a relatively simple model known as monoclinic transpression to characterize deformation in the San Andreas fault borderlands (Fig. 3A; Fossen and Tikoff, 1993). This representation of transpression assumes vertical boundaries and horizontal motion, which are both conditions expected for a primarily strike-slip plate boundary (Dewey, 2002).

Monoclinic transpression simultaneously combines a coaxial, fault-perpendicular shortening k with a noncoaxial, fault-parallel shearing γ described by the following deformation (or position gradient) matrix from Tikoff and Fossen (1993):

$$\mathbf{F} = \begin{bmatrix} 1 & \dfrac{\gamma(k-1)}{\ln(k)} & 0 \\ 0 & k & 0 \\ 0 & 0 & k^{-1} \end{bmatrix}. \quad (1)$$

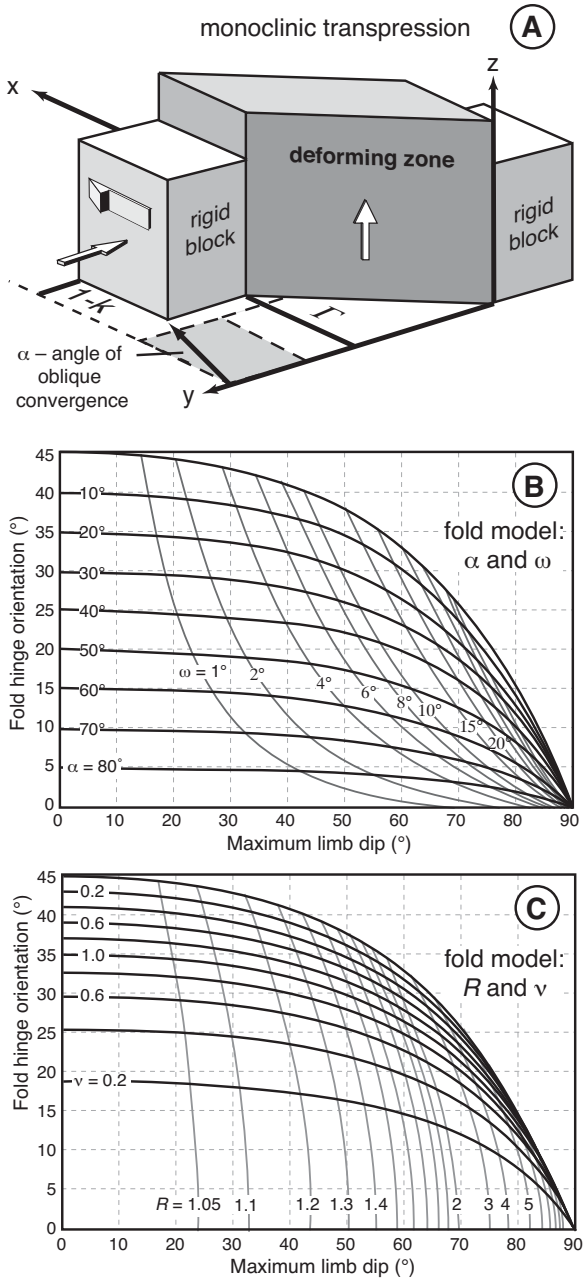

Figure 3. (A) Block diagram of monoclinic transpression illustrating parameters from Equation 1. (B) Determination of the magnitudes α and ω for combinations of our input parameters—fold hinge orientations and limb dips—and contour results. For α, the contour interval is 10°, where α = 0° for simple shear and α = 90° for pure shear, which is unlabeled but parallels the *x*-axis. For ω, we show 2° intervals for 2° ≤ ω ≤ 10°, and 5° increments for 10° < ω. (C) Calculation of the magnitudes of two strain parameters for combinations of our input parameters: *R*, the aspect ratio of the finite strain ellipse in the *x*-*y* plane strain, and ν, the shape factor of the finite strain ellipsoid given by $\nu = \dfrac{2\left(\ln(S_2) - \ln(S_3)\right)}{\ln(S_1) - \ln(S_3)} - 1$**, where S_i values are the magnitudes of the finite strain ellipsoid axes (Ramsay and Huber, 1983). For *R*, the contour interval is 0.1 for 1.1 ≤ *R* ≤ 2.0 with 1.0 intervals when 2.0 < *R*. For ν, the contour interval is 0.2; when ν = 0, deformation is plane strain, which occurs along the *x*-axis and along the path α = 0° from B. When ν > 0, deformation is characterized by flattening, as expected for transpression.**

Geological Society of America Bulletin, published online on 21 January 2011 as doi:10.1130/B30150.1

The $\mathbf{F}_{12}$ component is sometimes simplified as Γ (Fig. 3A). For our modeling, the coordinate system of **F** is aligned such that the *x*-direction is parallel to the San Andreas fault, the *y*-direction is perpendicular to the fault, and the *z*-direction is vertical. Because the $\mathbf{F}_{11}$ component is one, no shortening or lengthening occurs parallel to the San Andreas fault, and shortening perpendicular to the fault ($\mathbf{F}_{22}$) is balanced exactly by vertical motion ($\mathbf{F}_{33}$).

Three useful calculations can be made from **F**. The style of transpression can be determined from the angle of oblique convergence, denoted α, which represents the movement direction between the two rigid blocks on either side of a deforming zone (Fig. 3A). This angle is defined by Fossen et al. (1994) as

$$\alpha = \tan\left(\frac{\ln k}{\gamma}\right)^{-1}. \quad (2)$$

When α = 90°, deformation is purely coaxial; when α = 0° deformation is purely noncoaxial. If 0° < α < 90°, deformation is transpressional and includes both coaxial and noncoaxial components. By finding the velocity gradient matrix **L** from the deformation matrix **F**, a method described in more detail elsewhere (Tikoff and Fossen, 1993; Provost et al., 2004; Titus and Davis, 2009), we can compute the instantaneous stretching axes (ISAs). These orientations are of interest since they parallel the stress directions responsible for deformation. We also compute the bulk rotation of the system ω, which is due to the noncoaxial component of deformation (McKenzie and Jackson, 1983). The ω angles are useful for comparison with vertical-axis rotations derived from paleomagnetic data.

Folds in Transpression

To use map data from folds to characterize deformation, we must understand both the orientations in which folds initiate and the ways that folds behave during progressive deformation.

Physical and numerical models of folding in transpression demonstrate that fold hinges initially form perpendicular to the minimum (horizontal) ISA (Graham, 1978; Odonne and Vialon, 1983; Tikoff and Peterson, 1998). For a particular deformation, this is controlled by the angle of oblique convergence. For example, in our reference coordinate system, fold hinges form parallel to the San Andreas fault when α = 90°; progressive deformation causes fold tightening, but fold hinges remain parallel to the fault. In contrast, when α < 90°, folds form oblique to the fault strike, and progressive deformation causes rotation of the fold hinge about a vertical axis toward the shear direction (Wilcox et al., 1973).

If α < 90°, there are two ways to treat the rotation of fold hinges in map view. They may rotate passively as material lines, which means that material in the fold hinge remains in the fold hinge during progressive deformation. Alternatively, fold hinges may rotate as active markers that track the orientation of the finite strain ellipse during progressive deformation. The conclusions drawn from these two treatments of fold hinges do not differ greatly for moderate amounts of deformation and are often within the errors for estimating fold hinge orientations and limb dips from maps (see fig. 3 *in* Titus et al., 2007). In transpressional environments, active rotation is supported by field data (Bürgmann, 1991), theoretical models (Treagus and Treagus, 1981), and physical models of folding (Tikoff and Peterson, 1998). In fact, Tikoff and Peterson (1998) observed material lines rotating through fold hinges in their experiments of transpressional folding, which cannot occur if fold hinges behave as passive markers. We therefore assume active rotation of fold hinges for our modeling.

Using Folds to Determine the Deformation Matrix **F**

We use two pieces of information from folds across the region to solve for the two unknowns in the deformation matrix **F**. First, because we treat folds as active markers, the fold hinge orientation must parallel the long-axis of the finite strain ellipse. This orientation is the eigenvector associated with the largest horizontal eigenvalue of the Finger Tensor $\mathbf{FF}^{\mathbf{T}}$ (Flinn, 1979). Second, the limb dip is used to estimate the magnitude of the short axis of the finite strain ellipse following the method outlined in the appendix of Jamison (1991) and adapted slightly for active fold rotation. We assume each fold shape is upright and symmetric; each fold is approximated by a sine wave constrained by the maximum limb dip, which reflects the steepest part of the sine curve. We compute a line integral of this sine wave to determine the shortening, which constrains the square root of the smaller horizontal eigenvalue of $\mathbf{FF}^{\mathbf{T}}$. With one eigenvector and another eigenvalue, we are able to solve for **F**. There are usually two possible solutions, and we choose the one that is dextral and corresponds to transpression ($k < 1$). From **F**, we can determine α and ω as illustrated in the nomogram in Figure 3B, as well as the orientations of the ISAs. For reference, we have also shown how the aspect ratio and shape of the finite strain ellipsoid vary as a function of our model input data in Figure 3C.

Fold Data Set and Analysis

Fold hinges were digitized from 15′ quadrangles (Dibblee, 1971, 1972, 1975; Bartow, 1991) for regions adjacent to the central and southeast sections of the creeping segment (Fig. 4A). Because fold hinges vary in length and orientation, we divided each hinge into linear segments of equal length. We found that a 500 m segment length adequately characterized the level of detail on the original maps. The distance between the segment midpoint and the closest fault (either the San Andreas or Rinconada fault) was calculated, and each segment was assigned a limb dip based on the available map data. Although we used local maximum limb dips to constrain fold shapes, these still provide a minimum estimate of the total deformation because prefolding strain cannot be accounted for using folds as the only kind of strain marker (Jamison, 1991).

We smoothed natural variability in the map data by computing weighted average fold hinge orientations and weighted average limb dips on a regular 15 km fault-parallel grid superimposed over the study area (Fig. 4B). Each grid region is assumed to deform homogeneously, which allows us to compute the local deformation matrix **F**, the angle of oblique convergence α, and the ISAs. We then examine patterns of heterogeneous deformation across the region by contouring values of α (Fig. 4C) and by plotting the grid results for the ISAs (Fig. 4D).

Results

Folds flanking the Rinconada fault have similar orientations on either side of the fault (Fig. 4B), which creates symmetric α contours about the fault (Fig. 4C). However, the α angles vary along the fault strike. In the northwest, α < 30° is common; in the southeast, α increases to 45°–60° near the intersection with the Nacimiento fault. The orientations of the minimum ISAs are consistently oblique to the Rinconada fault (Fig. 3D).

Folds flanking the San Andreas fault do not display the same symmetry across the fault, although deformation is generally consistent along the fault strike. Folds to the southwest extend at most 10 km from the fault, with <10° between the fold hinge and the fault strike; this causes high α angles and minimum ISA orientations that are close to fault normal. Those to the northeast extend for up to 40 km from the fault, and the obliquity between the fold hinge and the fault strike varies with distance (Fig. 4B). Folds immediately adjacent to the fault have 10°–25° obliquities, those 15–30 km from the fault have 30°–40° obliquities, and those more than 30 km away are mostly parallel to the fault. The α angles and ISA orientations therefore form bands of consistent values reflecting the changing fold orientations; these bands are generally parallel to the fault strike.

Geological Society of America Bulletin, published online on 21 January 2011 as doi:10.1130/B30150.1

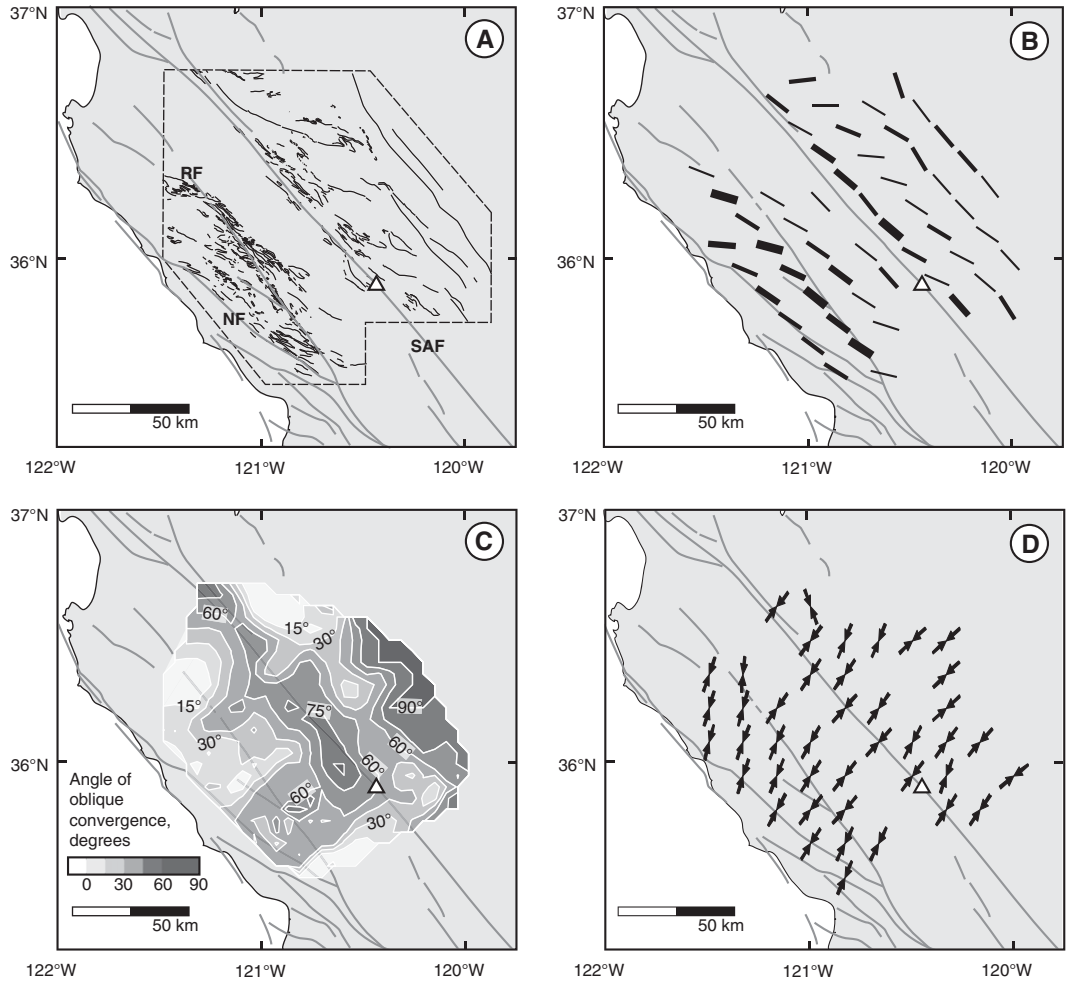

Figure 4. Maps of central California showing data and results of map-scale fold analysis. The dashed black line indicates the extent of fold analysis. (A) The fold hinges were digitized from Dibblee (1971, 1972, 1975) and Bartow (1991). (B) Weighted averages of fold hinge orientations on a 15 km grid. The line thickness is proportional to the sum of the weights of nearby folds used to calculate the weighted average. (C) Contour map of α on a 15 km grid. (D) The minimum horizontal instantaneous stretching axes (ISAs) calculated from the map data. Where there are not enough folds nearby to compute a weighted average, no arrows are drawn. The white triangle on each map indicates the location of the city of Parkfield, California. Faults are abbreviated as: NF—Nacimiento, RF—Rinconada, SAF—San Andreas.

Discussion of Results

By comparing the deformation patterns across these two faults, we begin to understand how large-scale geology can control the regional patterns of deformation. Because folds are symmetric across the Rinconada fault and asymmetric across the San Andreas fault, we suggest that the type (and strength) of basement rocks controls the ultimate distribution of deformation. The Rinconada fault passes through a former sedimentary basin on Salinian basement. The material properties of rocks are essentially the same on either side of the fault, and the width of the deforming zone is probably controlled by inherited basin geometries. In contrast, the San Andreas fault marks the contact between Salinian and Franciscan basement. Because Franciscan ultramafic and sedimentary rocks are likely weaker than Salinian granites, deformation is more intense northeast of the fault and spreads further from the fault than deformation to the southwest.

This type of detailed, map-scale analysis has never been attempted for central California. It provides a novel, spatial view of deformation that can be compared to GPS results from the same region. However, these are only semi-quantitative results; to extract true quantitative information would require verification from other data sets such as cross-section restorations. While field data adjacent to the Rinconada fault are consistent with our results (Titus et al., 2007; Crump et al., 2009), the model is not consistent with independent data sets from folds along the edge of the Great Valley, such as the Kettleman Hills and Coalinga anticlines. For these two large folds, our model predicts $80° < \alpha < 90°$ and fault-perpendicular minimum ISAs. With such a high angle of oblique convergence, these folds would remain parallel to the San Andreas fault during progressive deformation (Fig. 3B), experiencing neither vertical-axis rotation (ω) nor the hinge-parallel elongation that necessarily accompanies rotation. However, paleomagnetic data indicate that both folds have rotated 10°–24° (White, 1987; Tetreault, 2006), and numerous hinge-perpendicular normal faults along the crest of the Kettleman Hills North dome have accommodated hinge-parallel elongation (Woodring et al., 1940). Using Figure 3B, our predicted value for α only matches the observed ω rotations for extremely high limb dips, much higher than the actual ~30°–40° limb dips, demonstrating that no single progressive deformation event can explain the data from these folds. We revisit these anomalous folds in the main discussion section, where we propose a mechanism to better explain their growth and development.

Summing Displacement along Geologic Transects

The previous fold-based analysis demonstrates that borderland deformation includes both fault-parallel and fault-perpendicular components, as illustrated by $\alpha < 90°$ for most of the region. This method was only intended to show qualitative spatial patterns of deformation. In this section, we estimate the fault-parallel and fault-perpendicular displacements recorded by different types of geologic structures to better quantify off-fault deformation.

Geological Society of America Bulletin, published online on 21 January 2011 as doi:10.1130/B30150.1

Estimating Displacements

We examine geologic structures along four transects that stretch from the start of topographic relief along the western edge of the Great Valley to the Nacimiento fault (Fig. 5). Each transect is divided into subdomains with broadly consistent lithologic and fabric orientations, illustrated by different letters beneath the transect. The subdomains include: (a) en echelon folds, (b) noncylindrical folds, (c) homoclines at the scale of the transect, (d) faults with offsets (excluding those with poorly constrained, vertical displacements such as the Waltham Canyon fault), (e) undeformed rock, (f) not enough information to characterize deformation, and (g) large-map scale folds along the edge of the Great Valley. Transect locations were chosen to correspond with GPS velocity profiles presented later and to avoid regions with large group f domains where deformation was difficult to quantify.

In group a domains of en echelon folding, we calculate the fault-parallel and fault-perpendicular components of deformation following the method outlined in the previous section. To estimate error bars associated with these displacements, we use a small range of fold hinge orientations and limb dips representative of each subdomain. For group b domains with noncylindrical folds, we treat each fold limb separately and halve the deformation computed from our fold model. For group c domains of homoclinal deformation, we use a trigonometric approach that compares the angular difference between the homocline strike and the San Andreas fault to find the component of fault-parallel deformation. To find the fault-perpendicular component, we use the average apparent dip and length of the domain. For group d domains of map-scale faults, we decompose offset bedding contacts into their fault-parallel and fault-perpendicular components (relative to the San Andreas or Rinconada fault strikes) and sum the components (Wojtal, 1989). In group f domains where deformation is clearly recorded in the rocks (for example, elongated serpentine stringers in Fig. 5), but was impossible to quantify without more detailed field measurements, we assume that no deformation occurred. No transects had more than 15% of their total length in this type of subdomain. Finally, for group g domains with large-map scale folds, we estimate percent shortening and elongation using the available data from the region including cross-section reconstructions (Namson and Davis, 1988; Medwedeff, 1989; Wentworth and Zoback, 1989; Wickham, 1995), paleomagnetic results (White, 1987; Tetreault, 2006), and geologic maps (Woodring et al., 1940).

Our calculations of displacements for group a and d domains are the most reliable. The en echelon fold model was calibrated with hinge-parallel elongation derived from small-scale fault populations and vertical-axis rotations from paleomagnetic data (Titus et al., 2007). Although we do not know whether the faults in group d domains also record vertical motion, the fault traces are typically straight in map view, suggesting vertical fault planes. Furthermore, two main orientations are observed: a large set of NNW-striking faults with right-lateral offsets and a smaller set of NE-striking faults with left-lateral offsets, consistent with R and R′ orientations, respectively. These observations suggest that the small-scale faults are strike-slip faults for which horizontal separations can be measured from maps. Displacement estimates for group b and c domains are probably oversimplified, but they are generally consistent with the deformation pattern recorded along adjacent sections of each transect. For group g domains, the magnitude of fault-perpendicular shortening is more easily estimated than that for fault-parallel elongation. Depending on the fold in question, shortening estimates vary between 5% and 15%, and hinge-parallel elongation vary between 1% and 5%, except for the Coalinga anticline, where we estimate 2%–10% elongation because of the paleomagnetic data (Tetreault, 2006). Because we could not account for offsets along subparallel thrust faults, such as the Waltham Canyon fault, nor deformation from group f domains, these cumulative displacements represent minimum estimates.

Cumulative Displacements

In Figure 6, we sum the fault-parallel and fault-perpendicular components of deformation starting on the northeast side of each transect. Each point represents the average deformation estimated from a single subdomain, which is why the distance between points and total number of points varies for different transects. The error bars reflect the maximum and minimum values based on our ability to bracket deformation for particular subdomains. For ease of comparison, the graphs from all transects are aligned with the San Andreas fault. Noteworthy characteristics of specific transects are discussed next.

Northeast of the San Andreas fault, displacements from the NW and central transects can be fit with a relatively straight line, whereas the SW and Carrizo transects show a more pronounced curvature. This suggests that deformation is more evenly distributed in the northern two transects, while deformation is concentrated closer to the San Andreas fault in the southern two transects. For all four transects, displacements across the Rinconada fault can each be fit with a relatively straight line, although the slope of that line varies between transects; the greatest displacements are accommodated across the Carrizo transect, and the least are across the SW creeping segment.

All transects show cumulative displacements of 10–14 km with two exceptions: the ~8 km fault-perpendicular displacement for the NW creeping segment and the ~8 km fault-parallel displacement for the central creeping segment. We suggest that these lower estimates are related to difficulties in characterizing deformation in these transects. For the NW creeping segment, we could not quantify deformation in the group f domain closest to the Great Valley (Fig. 5). The obliquity of bedding in this area is not easily reconciled with a dextral strike-slip fault system, and therefore we did not apply any method to characterize deformation. Further, this region has several thrust faults that clearly accommodate shortening but do not have well-defined offsets (Fig. 5; e.g., Lettis, 1985). Similarly, the fault-parallel displacement from the central creeping segment is likely underestimated due to three particular subdomains: the Franciscan rocks immediately northeast of the San Andreas fault, Quaternary sediments southwest of the Rinconada fault that may obscure geologic structures, and our estimate of 2%–10% hinge-parallel extension in the Coalinga anticline. If we could better characterize deformation across these two transects, we suggest the cumulative displacements would better match the estimates from the three other transects.

Comparison with Other Studies

Displacement estimates across the Rinconada fault can be compared to several studies that used folds to estimate the kinematics of deformation. Along the NW creeping segment transect, the present method determined ~2.5 km of fault-parallel displacement. This is consistent with the 2.3–5.0 km estimate from Titus et al. (2007), based on a slightly different summation method, as well as the ~2 km estimates from the map-based approach of Jamison (1991) and Krantz (1995). The fault-perpendicular estimate of ~2.5 km is also consistent with the results from these studies.

Displacements northeast of the San Andreas fault can be compared to cross-section reconstructions that rely on seismic data. This comparison is only possible for the fault-perpendicular component, since these models assume that there is no fault-parallel component of deformation. Near our central creeping transect with ~9 km of shortening, Namson and Davis (1988) estimated 11 km of shortening for a longer cross section that extended further into the Great Valley than our transect. Across the Kettleman Hills portion of our SE creeping transect with ~4 km, Bloch et al. (1993) found

Geological Society of America Bulletin, published online on 21 January 2011 as doi:10.1130/B30150.1

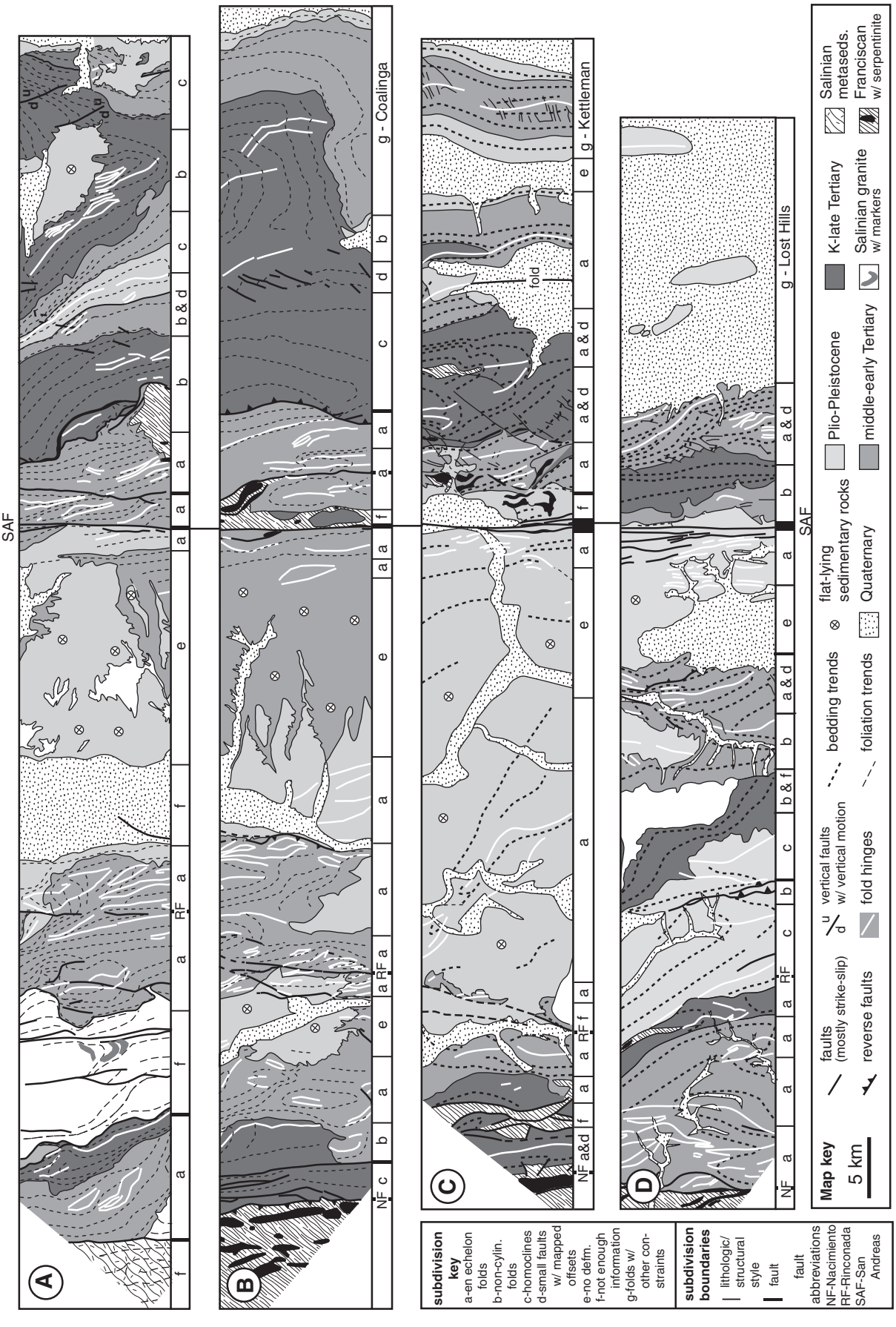

Figure 5. Four transects, each 12.5 km wide, used in our quantitative displacement analysis. Refer to Figures 1 and 2 for transect locations. The transects are aligned vertically so that the San Andreas fault is in the same approximate location for all four transects. The letters and divisions beneath each transect refer to subdomains described in more detail in the text. Transects were compiled from mapping by Dibblee (1971, 1972, 1975; Dibblee et al., 1999; Dibblee-Foundation, assorted years).

Geological Society of America Bulletin, published online on 21 January 2011 as doi:10.1130/B30150.1

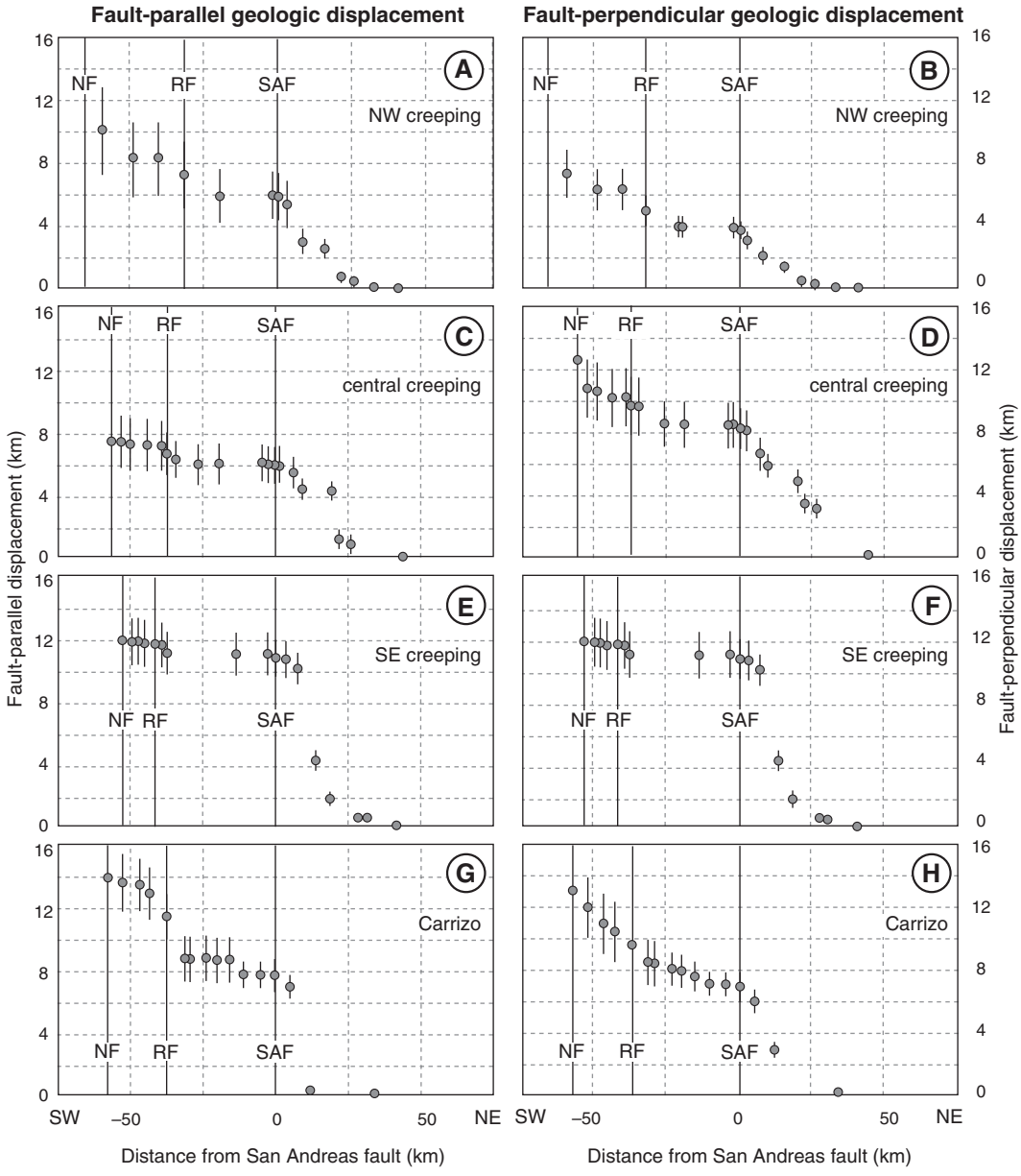

Figure 6. Off-fault deformation quantified from the four geologic transects in Figure 5. Fault-parallel components are shown in the left column; fault-perpendicular components are in the right column. Each data point represents the deformation estimated in a single subdomain. Note that the error bars become progressively larger to the southwest because displacements were summed cumulatively from the northeast. Faults are abbreviated as: NF—Nacimiento, RF—Rinconada, SAF—San Andreas.

~3.7 km of shortening, of which 2.3 km occurred in the past 2.5 m.y. Near the Lost Hills portion of our Carrizo transect with 3.5 km, Medwedeff (1989) found 4.5 km of shortening. Thus, our fault-perpendicular displacements are generally consistent with those derived from very different types of kinematic models.

We can compare our cumulative estimate of ~12 km of fault-perpendicular displacement with two independent estimates of total shortening across the region. Argus and Gordon (2001) used topography coupled with an Airy model of isostatic compensation as a proxy for shortening, estimating that ~15 km of fault-perpendicular displacement is required to match the topography across the portion of the plate boundary above sea level. Namson and Davis (1988) extended their fault-bend fold model across the Coast Ranges, estimating 33 km of fault-perpendicular shortening. Our results are consistent with the former estimate and much lower than the latter, which we suggest is too high for several reasons. First, Namson and Davis (1988) did not account for the distinct change in deformation style on Franciscan and Salinian basement on either side of the San Andreas fault. Of the 33 km of shortening, 22 km are inferred to have accumulated on regions with Salinian basement near faults that have less total displacement than the San Andreas fault. Second, their model assumes that borderland deformation is characterized by only fault-normal shortening with no fault-parallel elongation. This leads to an overestimate of the total fault-perpendicular displacement and no estimate of fault-parallel displacement (Teyssier and Tikoff, 1998). Last, to develop the observed topography across the creeping segment at the present fault-normal plate motion rate, the 33 km shortening estimate would require 7–18 m.y. (Argus and Gordon, 2001), much longer than is supported by the timing of the Coast Range orogeny (Page et al., 1998).

Implications of this Analysis

There are several important implications of this analysis. First, the magnitudes of cumulative fault-parallel and fault-perpendicular displace-

Geological Society of America Bulletin, published online on 21 January 2011 as doi:10.1130/B30150.1

ments are approximately equal. This is contrary to the common viewpoint about borderland deformation in central California, which often assumes that these regions only record fault-perpendicular shortening (Mount and Suppe, 1987; Zoback et al., 1987). Second, the magnitude of off-fault deformation is approximately the same across both creeping and locked segments of the fault, suggesting that long-term distributed deformation is similar across central California despite the difference in fault behavior. Third, the distribution of geologic displacements is uneven across the region and appears to be related to basement type. At least half, and perhaps up to two-thirds, of each total displacement is accommodated northeast of the San Andreas fault on Franciscan basement. The remainder is accommodated adjacent to the Rinconada fault; displacements are absent between the two major faults where Salinian basement is often at or near the surface. Last, deformation is more smoothly distributed northeast of the fault for the two northern transects and is accommodated by large-scale folding. In contrast, deformation is more narrowly confined in the southern transects (<25 km from the fault) and primarily accommodated by subsidiary strike-slip faults that are oblique to the San Andreas fault.

Displacement Rates

To compare these estimates of geologic deformation to short-term GPS deformation described in the following section, we convert our geologic displacements (~12 km for both fault-parallel and fault-perpendicular components) to displacement rates. Such a conversion is challenging because geologic structures record deformation over long time scales and can result from complex patterns of deformation and changing kinematics over time. We thus make simplifying assumptions about the timing of deformation to produce a range of displacement rates that bracket the likely lower and upper limits on the long-term deformation rates in the borderlands.

Most off-fault deformation recorded by folds and other structures probably occurred since the relative shift in plate motion to oblique convergence that favored uplift and shortening within the Coast Ranges. This shift is bracketed between 8 Ma (Atwater and Stock, 1998) and 3.5 Ma (Pollitz, 1986; Page et al., 1998), suggesting that geologic structures between the Great Valley and the Nacimiento fault record ~1.5–3.5 mm/yr displacement rates. We suggest that the faster rates are more likely based on three lines of reasoning.

First, deformation intensified in many parts of central California in the Pliocene (Taliaferro, 1943; Page et al., 1998). For example, folds hinges near the Rinconada fault are in Miocene- and Pliocene-age rocks (Dibblee, 1976), suggesting that folding occurred after the Pliocene rocks were deposited. Bloch et al. (1993) found that 80% of the shortening across the Kettleman Hills South Dome region was accommodated in the last 2.5 m.y. Wentworth and Zoback (1989) suggested that the primary uplift of Kettleman Hills and other Great Valley folds has been in the past 2 m.y. Thus, much of the geologic evidence for deformation has occurred more recently than the 8 Ma estimate for the shift in plate motion (Atwater and Stock, 1998).

Second, we have not captured all the deformation recorded by geologic structures, and our cumulative estimates are minimum values. For example, we could not quantify deformation at scales finer than the 15′ map scale, contributions from regional structures such as the Waltham Canyon fault, deformation in clearly deformed Franciscan rocks or other group f subdomains, or deformation under valleys or along other buried structures.

Third, we have better constraints on the timing of folding adjacent to the Rinconada fault (Dibblee, 1976), which hint at the faster values for displacement rates. Fold hinges are parallel in sedimentary rocks of Miocene and Pliocene ages, suggesting that folding occurred in the last 5 m.y. after the Pliocene rocks were deposited. These folds record 2.5–5 km of fault-parallel displacements (Titus et al., 2007), suggesting a displacement rate of 0.5–1 mm/yr. The displacement rate recorded by geologic structures northeast of the San Andreas fault should be equal to or likely higher than that recorded adjacent to the Rinconada fault because: (1) the shape of geologic displacement gradients across central California (Fig. 6) indicates that deformation is concentrated northeast of the San Andreas fault on Franciscan basement, and (2) the San Andreas fault has had an order of magnitude more total displacement than the Rinconada fault, suggesting that higher off-fault displacement rates might be expected adjacent to this fault. Thus, we suggest that geologic structures between the Nacimiento fault and the edge of the Great Valley record the higher end of the 1.5–3.5 mm/yr displacement rate range for both fault-parallel and fault-perpendicular components.

SHORT-TERM DEFORMATION FROM GPS DATA

GPS Data

Data Processing Methods

We used data from 102 continuous and 48 campaign GPS stations to quantify the velocity field across central California. Data for these stations begin as early as the mid-1990s and extend through May of 2009.

We analyzed daily and campaign GPS data with GIPSY software from the Jet Propulsion Laboratory (JPL) and AMBIZAP software to resolve phase ambiguities (Blewitt, 2008). We used a precise point-positioning strategy (Zumberge et al., 1997) and fiducial-free satellite orbits and clock corrections from JPL (Heflin et al., 1992) to estimate daily, no-fiducial station coordinates. The loosely determined, daily station coordinates were transformed to ITRF2005 (Altamimi et al., 2007) using daily seven-parameter Helmert transformations from JPL. Common-mode noise in the GPS time series was estimated from the time series of well-behaved, continuous stations within and external to our study area and removed from coordinate time series for all sites (Márquez-Azúa and DeMets, 2003). The final coordinate time series have daily repeatabilities of 1–2 mm in latitude and 2–3 mm in longitude.

After processing the raw GPS data, we estimated GPS station velocities via linear regression of the station coordinates, including any known or estimated offsets due to hardware or other changes at individual GPS stations or due to earthquakes. The coseismic and postseismic offsets caused at our continuous stations by the 2003 San Simeon and 2004 Parkfield earthquakes were estimated and removed as part of our linear regressions of their coordinate time series (details are provided in the GSA Data Repository[1]). At stations with only infrequent campaign measurements, we used offsets predicted from the elastic deformation models for the coseismic and postseismic effects of the two earthquakes (Johanson et al., 2006) to correct the site coordinate time series.

Uncertainties in the GPS station velocities were determined using an empirically derived error model that accounts for different noise components in the GPS time series (Mao et al., 1999) and includes uncertainties propagated from the covariances of the angular velocity vectors described later in this paper. The velocity uncertainties do not include any additional uncertainty due to the imperfectly known earthquake-offset corrections described previously and therefore likely understate the true uncertainties. The possible bias in a station's velocity due to the imperfect corrections for the effects of the two earthquakes depends on the particulars of its location relative to each of the two rupture zones as well as the specific time period

[1]GSA Data Repository item 2011010, additional information about the global positioning system station velocities used in this study, is available at http://www.geosociety.org/pubs/ft2010.htm or by request to editing@geosociety.org.

Geological Society of America Bulletin, published online on 21 January 2011 as doi:10.1130/B30150.1

spanned by the site. Numerical experiments with our GPS time series suggest that the likely bias is smaller than 1 mm/yr at most sites flanking the central creeping segment, where most of our stations are located, but may be as large as 2 mm/yr for stations within 20 km of the San Simeon and Parkfield ruptures, where the transient postseismic effects of the two earthquakes may contribute significantly to the site motions for years after the earthquakes. We thus exercise caution in interpreting the velocities of stations near either of the rupture zones.

TABLE 1. BEST-FITTING GLOBAL POSITIONING SYSTEM (GPS) ANGULAR VELOCITY VECTORS

Plate	*N*	Lat.	Long.	ω (°/m.y.)	σ_{xx}	σ_{yy}	σ_{zz}	σ_{xy}	σ_{xz}	σ_{yz}
					($\times10^{-8}$ radians^2/m.y.^{2})					
SNGV-ITRF05	32	7.8°S	111.9°W	0.289	15.4	42.1	36.3	25.5	–23.6	–39.1
PA-ITRF05	27	63.5°S	110.7°E	0.676	0.11	0.03	0.04	0.02	–0.01	0.00
SNGV-PA	60	46.0°N	90.0°W	0.787	15.5	42.2	36.3	25.5	–23.6	–39.1

Note: Abbreviations: SNGV—Sierra Nevada–Great Valley block; PA—Pacific plate. Angular velocity vectors specify counterclockwise rotation of the first named plate relative to the fixed (2nd) plate around the specified pole coordinates. The Cartesian angular velocity covariances are specified in the last six columns. *N* indicates the number of GPS stations that were used to determine the best-fitting angular velocity vector. The station velocities used to determine these angular velocities are given in Tables DR1 and DR2 of the electronic supplement (see text footnote 1).

Pacific Plate and Sierra Nevada–Great Valley Reference Frames

Using Sierra Nevada–Great Valley block boundaries adapted from Dixon et al. (2000), we determined the motion of this block relative to ITRF2005 from the velocities of 32 continuous stations for which we processed daily data (see the supplemental material for more information about GPS station velocities and reference frames [see footnote 1]). The location and residual motions of each of the 32 sites (supplemental Fig. DR1 [see footnote 1]) define a self-consistent set of velocities with a weighted root-mean-square misfit of their best-fitting angular velocity vector (supplemental Table DR1) of 0.9 mm/yr, close to the estimated velocity uncertainties. The velocities of 27 continuous stations from locations in the interior of the Pacific plate (supplemental Fig. DR2 and Table DR2 [see footnote 1]) were used to estimate the best-fitting Pacific plate angular velocity vector (Table 1) and have a weighted root-mean-square misfit of 1.2 mm/yr, also close to the estimated station velocity uncertainties.

The angular velocity vector that best describes the motion of the Sierra Nevada–Great Valley block relative to the Pacific plate (Table 1) predicts motion of 36.9 ± 0.3 mm/yr toward N32.6°W ± 0.4° near the center of our study area (36.2°N, 120.7°W), ~8° clockwise from the N41°W strike of the San Andreas fault in central California. When rotated onto the azimuth of the San Andreas fault, our new angular velocity predicts fault-parallel dextral motion of 36.5 ± 0.2 mm/yr and fault-perpendicular shortening of 5.4 ± 0.3 mm/yr. For comparison, the motions predicted by the Sierra Nevada–Great Valley–Pacific angular velocity vectors of Argus and Gordon (2001) and d'Alessio et al. (2005) are 38.8 ± 2 mm/yr, N36.1°W ± 2°, and 37.9 ± 0.6 mm/yr, N34.2°W ± 0.8°, respectively, which are faster than predicted by our new estimate and more parallel to the San Andreas fault. The 3.0 ± 2.0 mm/yr (1σ) and 1.4 ± 0.7 mm/yr (1σ) respective vector differences between our new and these previous estimates are not, however, significant at the 95% confidence level.

Velocity Field in Central California

We present the velocity field from central California in two different frameworks: in standard geographic orientation (Fig. 7) to facilitate comparison with the geologic data presented in Figure 4, and as a San Andreas fault–parallel oblique Mercator projection (Fig. 8) plotted with local seismicity data.

The motions of GPS sites southwest of the fault are nearly parallel to, but slightly convergent with the San Andreas fault when all station velocities are plotted relative to the Sierra Nevada–Great Valley block (Fig. 7A). This pattern is consistent with the predictions of our new and previous Sierra Nevada–Great Valley–Pacific plate angular velocity vectors for 3–5 mm/yr of fault-normal motion in central California. To better emphasize the details of short-term deformation on both sides of the San Andreas fault, we subtract Pacific plate motion from stations southwest of the fault (Fig. 7B). In this plot, broad patterns emerge on both sides of the fault that are spatially correlated with the changing slip style along the fault strike. Northeast of the fault, velocity vectors adjacent to the central creeping segment are slower (<5 mm/yr) and more N-directed than those adjacent to the southeast creeping segment (5–10 mm/yr); the transition between these two different velocity domains is rapid. Southwest of the fault, velocity vectors adjacent to the creeping segment are slower (3–7 mm/yr) and directed 20°–35° oblique to the fault strike, in comparison to faster (>10 mm/yr) fault-parallel velocities adjacent to the southeast creeping segment.

In Figure 8, the slowing velocity vectors northeast of the fault (the upper half of Fig. 8), which cause differential convergent motion, occur across the Coalinga and Kettleman Hills anticlines and coincide with the broad seismic zone north of Parkfield. Southwest of the fault (lower half of Fig. 8), little seismicity occurs immediately adjacent to the San Andreas fault. However, a similar zone of convergence is observed near the San Simeon seismic zone. The velocity vectors across this region are consistent with the NE-SW shortening that was accommodated by reverse faulting that occurred during the 2003 M_w 6.5 San Simeon earthquake (Hardebeck et al., 2004).

Velocity Profiles across Central California

The fault-parallel and fault-perpendicular components of the GPS site velocities are plotted in Figure 9. The data were projected from a swath across the fault (Figs. 1 and 8) onto a single fault-normal transect for the northwest, central, and southeast creeping segments, and the Carrizo plain segment. These four transects roughly coincide with the geologic displacement gradients from Figure 6. (The slight mismatch between transects, especially for the third across the SE creeping segment, was necessary because a large section of Franciscan serpentinite is exposed near Parkfield, which would result in a less accurate estimate of geologic displacement.)

The fault-parallel velocity components plotted relative to the Sierra Nevada–Great Valley block (left column of Fig. 9) highlight the changing behavior of the San Andreas fault along strike. The motions of stations across the Carrizo transect vary smoothly across the fault and exhibit the sigmoidal shape consistent with elastic strain that accumulates adjacent to a locked fault. In contrast, the velocities of GPS stations adjacent to the creeping segment change suddenly at the San Andreas fault, offering clear evidence for varying amounts of fault creep. These partially to fully creeping transects also show an additional 4–6 mm/yr of motion on either side of the fault over distances of 50 km or more.

Three of the four transects also clearly exhibit gradients in their fault-perpendicular velocity components (right column of Fig. 9), totaling up to 4–6 mm/yr along their 100 km or longer lengths. These observed station motions are consistent with the 3–5 mm/yr predicted at this latitude for a fault striking N41°W by our own Sierra Nevada–Great Valley–Pacific plate angular velocity (Table 1) and thus indicate that most or all of the predicted contractional deformation between these two plates is accommodated within 100 km of the San Andreas fault.

The Parkfield transect, however, shows little evidence of shortening (Fig. 9F), consistent with

Geological Society of America Bulletin, published online on 21 January 2011 as doi:10.1130/B30150.1

results from other recent geodetic studies in that region (e.g., Shen and Jackson, 1993; Murray et al., 2001). This transect is the shortest of the four, extending <25 km northeast of the fault and only 75 km in total, in contrast to three longer transects across central California. Southwest of the San Andreas fault, the fault-normal component of the GPS station velocities gets smaller with distance from the fault (Fig. 9F); this trend is opposite of that observed for the transects farther to the northwest (Figs. 9B–9D). More than half of the stations in this transect southwest of the fault are located within 25 km of the rupture zones of the 2003 San Simeon and 2004 Parkfield earthquakes. The effects on their estimated velocities from the incompletely modeled postseismic transient effects of those two earthquakes may be as large as 2 mm/yr (see previous discussion). We therefore place little emphasis on the anomalous fault-normal velocity pattern for this transect.

Velocity Gradients and Reference Frames

Because the velocities of GPS sites from the San Andreas fault borderlands were not used to estimate either Pacific plate or Sierra Nevada–Great Valley block motion, we use them in Figure 9 to test the accuracy of the angular velocities from Table 1 and compare our plate motion model with those of Argus and Gordon (2001) and d'Alessio et al. (2005).

Throughout the study area, the two other models predict rates of fault-normal contraction that are 2–4 mm/yr slower than the fastest measured rates. Both models thus underestimate the fault-normal component of motion between these two plates. Our new Sierra Nevada–Great Valley–Pacific plate angular velocity better predicts the measured fault-normal rates, but still predicts rates that are 1–2 mm/yr slower than the most rapid measured rates along two transects. Similarly, our new angular velocity predicts velocities with fault-parallel components that agree better with the maximum measured fault-parallel velocities, particularly along the central creeping segment (Fig. 9C), where the absence of any elastic deformation associated with the San Andreas fault simplifies the comparison.

Strain Rate Analysis

Methodology

To better compare and contrast our geodetic and geologic measurements of off-fault deformation, we calculated instantaneous strain rate tensors from the GPS velocity field. These tensors are invariant to the reference frame to which the GPS velocities are referred and are thus free from possible biases related to a particular realization of the Sierra Nevada–Great Valley or Pacific plate reference frame. The orientations of strain rate axes are thus well suited for a comparison to the ISAs derived from our fold-based analysis (Fig. 4D). Drawbacks to this approach include correlations that are introduced between adjacent strain rate tensors that are estimated from spatially overlapping sets of GPS velocities, as well as variations in the strain rate tensors due to the heterogeneous station spacing.

We used the gridded, distance-weighted approach of Allmendinger et al. (2007) to invert GPS velocities for the velocity gradient tensor at nodes defining a regular grid in central California. Our node spacing of 9 km approximates the average station spacing in the field area. The velocity gradient tensor at each node is calculated from the surrounding GPS velocities. The importance or weight, *W*, of each GPS datum in the solution depends on its distance *d* from the grid node and a smoothing factor β (Shen et al., 1996), as follows:

$$W = e^{\frac{-d}{2\beta^2}}. \quad (3)$$

Undersmoothing the solution results in noisy velocity gradient tensors for grid nodes that sample only a few GPS stations. Conversely, oversmoothing the solutions undersamples the spatial density of the GPS network, resulting in overly smooth strain rate patterns. We chose our smoothing factor based on trial and error; with β = 12 km, the impact of noisy data was reduced without sacrificing many details in the strain rate patterns.

The weights *W* were used to create a diagonal weighting matrix **W**, which was inverted using a standard formulation (Menke, 1984) for a linear inverse problem

$$\mathbf{m} = \left[\mathbf{G}^{\mathrm{T}}\mathbf{W}\mathbf{G}\right]^{-1}\mathbf{G}^{\mathrm{T}}\mathbf{W}\mathbf{d}, \quad (4)$$

where **G** is a design matrix relating GPS station velocities to the velocity gradient tensor at a given location within the GPS network, **m** is a vector that contains the entries of the velocity gradient tensor, and **d** is a vector that contains the GPS velocity data. The construction and form of **G**, **m**, and **d** are described in detail by Allmendinger et al. (2007).

At each node, we decompose the velocity gradient tensor into a strain rate tensor and a vorticity tensor. From the eigenvalues and eigenvectors of the strain rate tensor, we calculate the dilatation rate and ISAs for that grid node (Allmendinger et al., 2007). Positive dilatation corresponds to horizontal extension that should be balanced by vertical thinning (subsidence). Negative dilatation corresponds to horizontal contraction that should be balanced by vertical thickening.

Results

Figure 7D shows the orientations of the ISAs and dilatation rates calculated from our observations at GPS stations throughout the region. Throughout the study area, the strain axes that correspond to shortening (blue lines) generally strike N-S, ~45° oblique to the San Andreas fault and consistent with those expected for a NW-striking, dextral fault. The most robust features of the strain rate pattern, as determined by their geographic area and the numbers of GPS stations that define them, consist of a region of prominent contraction north of Parkfield with dimensions ~60 km east-to-west and 30 km north-to-south (i.e., the blue area labeled "C region" in Fig. 7D) and a region of prominent extension southwest of Parkfield with dimensions ~50 km east-to-west and 40 km north-to-south (i.e., the red area labeled "E region" in Fig. 7D). The contractional region results from the progressive decrease and clockwise rotation of velocities exhibited by GPS stations on the Sierra Nevada–Great Valley block north and northwest of Parkfield (Figs. 7B and 8). The extensional region results from the progressively faster motions of GPS stations on the Pacific plate adjacent to the creeping segment southeastward from the locked Carrizo Plain fault segment (Figs. 7B and 8).

Other possibly significant variations in the strain rate pattern also emerge from the GPS velocity field, particularly in areas with numerous GPS sites that flank the creeping segment. In particular, an elongate region of low or zero dilatation extends ~50 km parallel to the San Andreas fault northeast of the creeping segment (labeled "N region" in Fig. 7D), where GPS velocities exhibit no apparent spatial variations (Figs. 7A–7B and 8). This agrees with previous reports of low strain rates northeast of the central creeping segment from Electronic Distance Meter (EDM) and GPS observations (Rolandone et al., 2009; Savage, 2009).

Using a different technique for estimating spatially averaged strain rate tensors, Hackl et al. (2009) derived a dilatation rate field for central (and southern) California from many fewer GPS stations than are used in this study. Although their strain rate pattern in central California (shown in their fig. 6) is similar to ours in some respects, the most prominent and robust feature of our strain rate pattern, the contractional region north of Parkfield, is weak or absent in the Hackl et al. (2009) solution. The reason for this difference is clear—their GPS velocity field lacks any stations northeast of the creeping segment of the San Andreas fault, which are essential for defining the fault-parallel velocity gradient that is the basis for identifying the region of contractional dilatation northwest of Parkfield.

Geological Society of America Bulletin, published online on 21 January 2011 as doi:10.1130/B30150.1

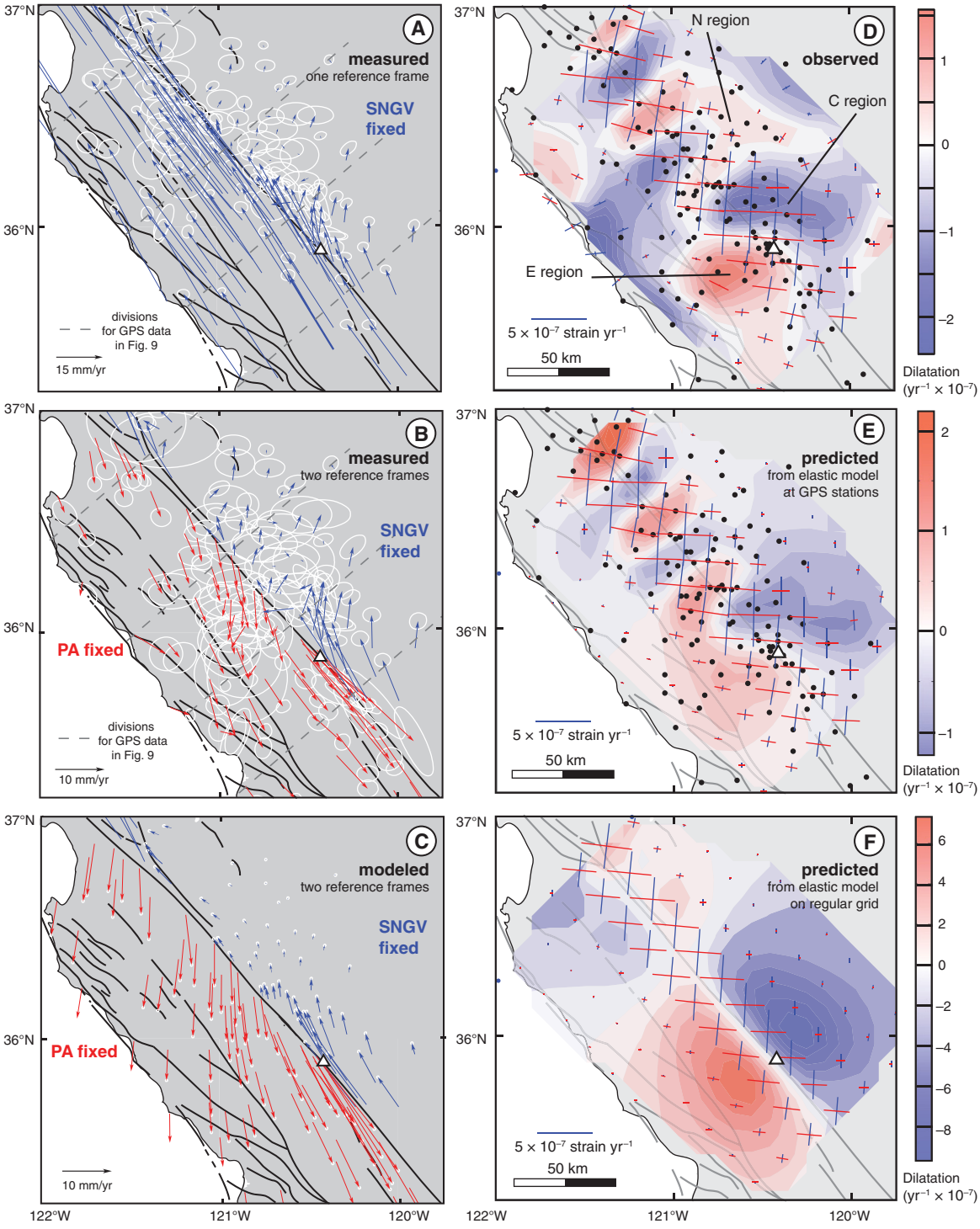

Figure 7. (A) GPS station motions relative to the SNGV microplate; error ellipses show 95% confidence intervals. (B) GPS station motions in two reference fames: relative to SNGV for sites northeast of the San Andreas fault and relative to the Pacific plate (PA) for sites southwest of the fault. (C) GPS station motions predicted by the elastic half-space model of Rolandone et al. (2008) in same reference frames as for B. (D) Strain rate distribution calculated from the velocity field with dilatation rates (colored contours), instantaneous stretching axes (blue lines – principal shortening, red lines – principal elongation), GPS station locations (black dots), and major faults. The labels point to areas of well defined contractional (C), extensional (E), and low-to-no (N) dilatational strain described in the text. (E) Strain rate distribution calculated from velocities predicted at the GPS station locations from an elastic half-space driven by the San Andreas fault slip rate distribution of Rolandone et al. (2008). (F) Strain rate distribution calculated from the same elastic half-space model as for part B, but from velocities predicted at uniformly spaced grid nodes throughout the study area. The white triangle on each map indicates the location of Parkfield, California.

Geological Society of America Bulletin, published online on 21 January 2011 as doi:10.1130/B30150.1

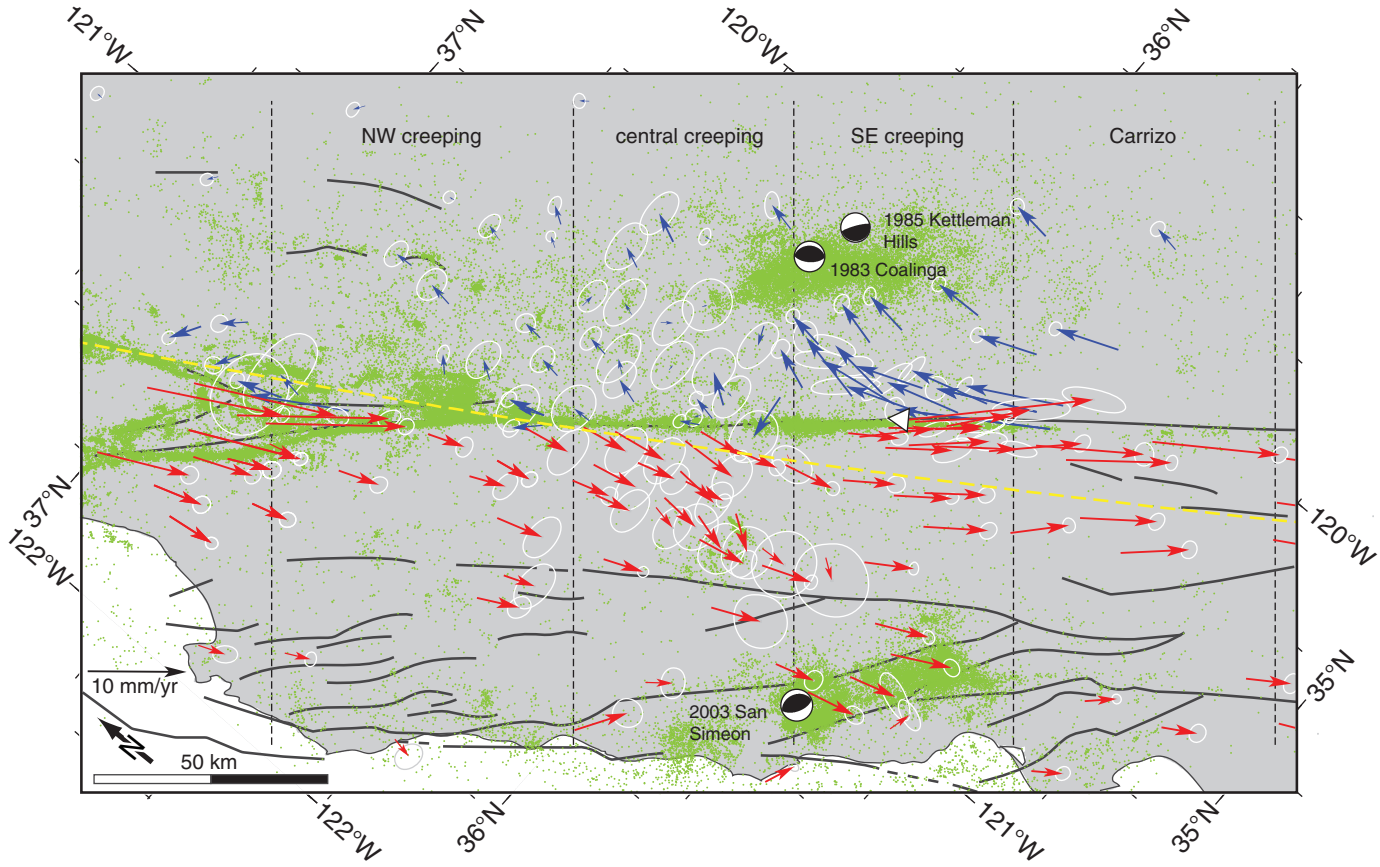

Figure 8. Oblique projection of GPS velocity field from Figure 7B and regional earthquake epicenters and focal mechanisms. The map equator has an azimuth of N41°W, parallel to the San Andreas fault. Earthquakes include all events with magnitude greater than 1 from 1972 to 2009 and are from the Northern California Earthquake Data Center. Focal mechanisms are Harvard Centroid Moment Tensor solutions for the period 1976–2009 and are limited to magnitudes greater than 6. GPS velocity uncertainties are 2-D, 1σ and are either relative to the Sierra Nevada–Great Valley microplate (blue) or the Pacific plate (red). Dashed yellow line is a small circle centered on the Sierra Nevada–Great Valley–Pacific pole from Table 1, which corresponds to the direction of instantaneous geodetic motion. Vertical dashed lines show the limits of the four GPS velocity transects.

Elastic Contribution of the San Andreas Fault

We next use forward elastic half-space modeling to illustrate that the pattern of strain rates shown in Figure 7D is consistent to first order with that expected for a locked strike-slip fault that incorporates a freely slipping segment. The modeling demonstrates that some of the strain rate patterns are robust, whereas others are likely artifacts of the nonuniform GPS station locations in the study area.

Predicted GPS Velocity Field

Our elastic half-space approximation for central California includes a single vertical strike-slip fault that represents the San Andreas fault. The model representation of the creeping segment of the San Andreas fault, which extends from San Juan Bautista to Parkfield and to depths of 12 km, is subdivided into smaller sections along strike and with depth, as shown by Rolandone et al. (2008). In addition to the shallow creep, the model includes slip on the San Andreas fault deep below and far to the northwest and southeast of the creeping segment. Analytical equations from Okada (1985) are used to determine the elastic response at each GPS site to slip rates that are imposed across each of the subfault segments. These slip rates correspond to the best-fitting slip-rate distribution determined by Rolandone et al. (2008) from an inversion of an earlier version of this GPS velocity field.

To first order, the velocity field predicted by our elastic model (Fig. 7C) matches the changing orientations and magnitudes of the observed GPS station velocities (Fig. 7B), which are important for defining the primary strain-rate features described in the previous section. The observed and predicted velocities, however, disagree in two primary respects. First, the predicted velocities southwest of the San Andreas fault gradually change from S- to SE-directed gradually adjacent to the central to SE creeping segment and are 7 mm/yr or faster. In contrast, the measured velocities are slower than the modeled velocities; their orientations abruptly change from S-directed adjacent to the central creeping segment to SE-directed near the SE creeping segment. Second, stations northeast of the fault and adjacent to the creeping segment are predicted to move more slowly and more parallel to the fault than is observed (compare blue velocities in Fig. 7C to Fig. 7B).

Predicted Strain Rate Pattern

We applied the strain rate analysis described in the previous section to two versions of the GPS velocity field predicted from our elastic

Geological Society of America Bulletin, published online on 21 January 2011 as doi:10.1130/B30150.1

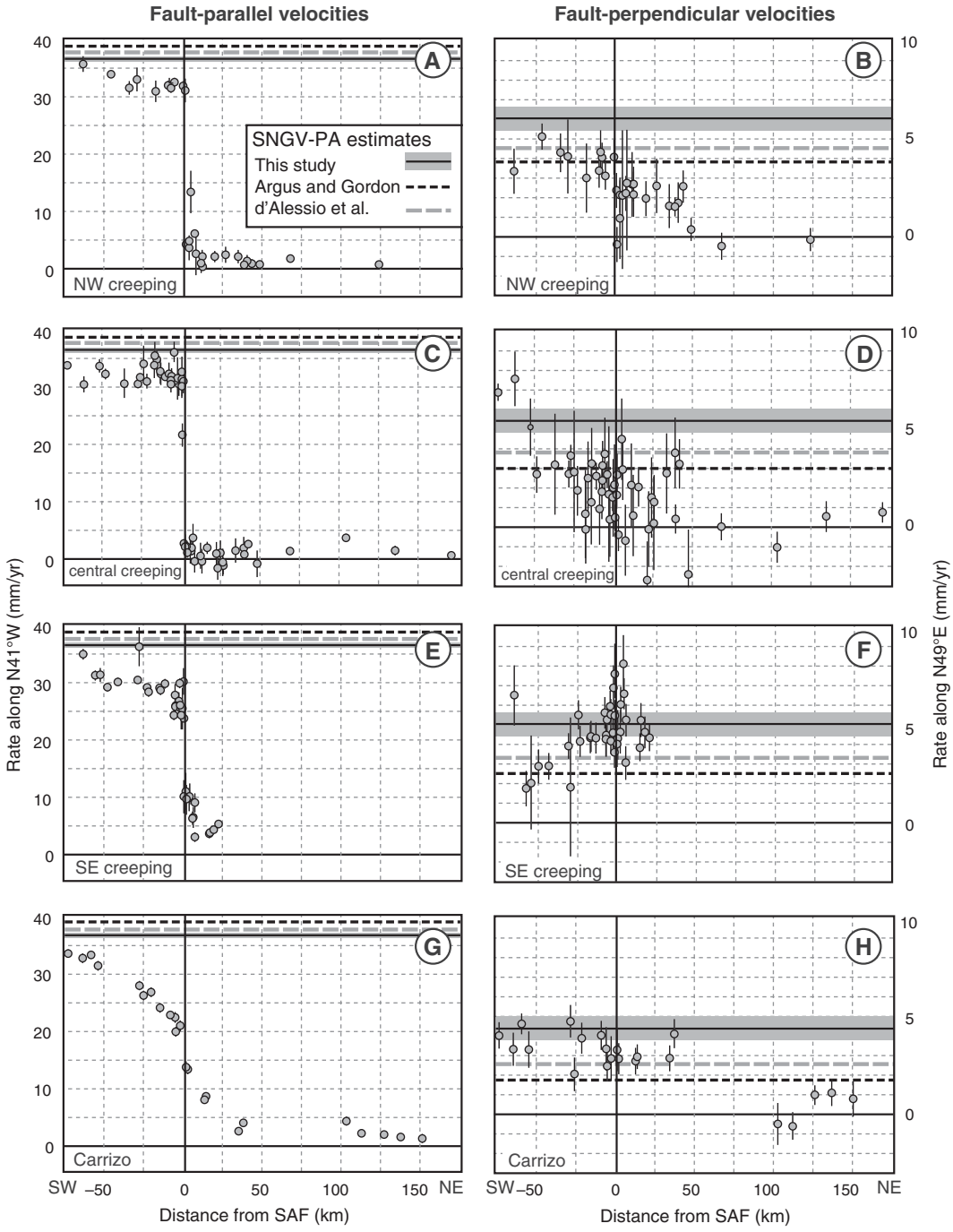

Figure 9. Components of GPS station velocities from Figure 7B rotated parallel (N41°W in left column) and orthogonal (N49°E in right column) to the San Andreas fault (SAF). Velocities were calculated relative to the Sierra Nevada–Great Valley block. The thin, solid black line shows our Pacific plate–Sierra Nevada–Great Valley block velocity predicted at the midpoint of each transect (with gray shading for 95% uncertainty). The dotted lines show the angular velocities for Argus and Gordon (2001), and d'Alessio et al. (2005). SNGV—Sierra Nevada–Great Valley, PA—Pacific.

modeling: one for velocities determined at the existing GPS station locations (Fig. 7E) and a second for velocities that define a hypothetical uniform grid within the study area (Fig. 7F). The predicted strain rate pattern for the former (Fig. 7E) closely matches the pattern of strain rates determined from our observed velocities (Fig. 7D). By implication, the GPS velocities are broadly consistent with the simple elastic half-space model described by Rolandone et al. (2008).

A comparison of the predicted strain rate patterns for the GPS station locations (Fig. 7E) and uniform grid (Fig. 7F) indicates that heterogeneous sampling of a large-scale pattern of deformation introduces artifacts into the resulting strain rate pattern, a point also emphasized by Allmendinger et al. (2007). By implication, some of the variations apparent in the observed strain-rate pattern (Fig. 7D) are likely to be artifacts of the uneven sampling provided by the present GPS network. For this reason, we focus on the large-scale patterns of contraction and extension described previously in this paper and do not interpret the secondary variations shown in Figures 7D–7E.

Conclusions from Velocity Field Modeling and Strain Rate Analysis

The observed GPS velocity field and pattern of strain rates derived from it are consistent with the predictions of our simple elastic half-space model. The velocities and strain rate patterns in

Geological Society of America Bulletin, published online on 21 January 2011 as doi:10.1130/B30150.1

our model are controlled by varying slip rates along a vertical strike-slip fault. suggesting that the first-order patterns in strain rates, with contraction northeast and extension southwest of Parkfield, are controlled by the locked to creeping transition along the San Andreas fault. Although the success of the simple elastic half-space model in matching the GPS velocity pattern suggests that future ruptures of adjoining segments of the San Andreas fault will relieve some or all of the spatially varying elastic strain that accumulates in the fault borderlands, we next describe evidence that permanent deformation in the fault borderlands may also relieve a significant fraction of the elastic strain.

COMPARISON OF LONG-TERM AND SHORT-TERM DEFORMATION

We compare geologic and geodetic rates of deformation from the four transects across the San Andreas fault as paired panels in Figure 10. The geologic displacements were transformed to displacement rates by assuming that all deformation occurred in the past 3 m.y., based on the major Pliocene–Pleistocene phase of geologic deformation (Page et al., 1998). The surficial fault creep rate was removed from GPS data southwest of the fault to display both fault-parallel and fault-perpendicular velocity gradients at the same scale (except panel E). For this reason, the fault-parallel gradient across the Carrizo plain was excluded because elastic strain dominates the signal, and no direct comparison can be made.

Four of the seven sets of panels, those for the northwest and central creeping segment (A–D), show broad agreement between the two data sets. The pair in panel E is also broadly consistent, but because the scales are quite different, we do not describe deformation for this panel in more detail. For panels A–D, geodetic deformation is confined to the region where geologic displacements accumulate and is not, for example, observed in the Great Valley. Both data sets demonstrate that at least half of the cumulative deformation accrues northeast of the San Andreas fault. The GPS velocities also suggest, within their uncertainties, that little or no deformation accumulates between the Rinconada and San Andreas faults on Salinian basement. We note, however, that the GPS velocities from transects across the creeping segment are too noisy to distinguish between the sigmoidal displacement rate distribution expected for a partly locked fault (such as those observed across the Carrizo plain by Schmalzle et al., 2006) and the slip-rate pattern for a fully creeping fault that lacks any contribution from elastic strain.

The two panels in this comparison that are least consistent (F–G) record the fault-perpendicular rates from the SE creeping and Carrizo transects. For both transects, shortening is recorded by the geologic data but is not presently observed in the GPS rates. We suspect that this is related to two factors. First, the GPS data from these transects only extend 25–40 km northeast of the San Andreas fault, compared to 50 km or more for the SE and central creeping segment transects. Thus, we may be missing some component of fault-perpendicular motion northeast of the GPS stations. Second, the GPS data southwest of the San Andreas fault show no fault-perpendicular shortening for the Carrizo segment and actually show fault-perpendicular lengthening for the Parkfield segment (i.e., fault-normal rates southwest of the San Andreas fault are slower than those northeast of the fault relative to Sierra Nevada–Great Valley). Both of these transects intersect the broad region of extension predicted from our strain rate modeling (Fig. 7F), possibly accounting for the apparent absence of shortening. In addition, the velocities of GPS stations located in the Parkfield transect may be affected by postseismic transient effects of the 2004 Parkfield and 2003 San Simeon earthquakes, both of which occurred within this transect (see supplemental material [see footnote 1]). Further work is needed to determine more reliably the pattern of fault-normal motions across the Parkfield transect.

DISCUSSION

The geologic and geodetic observations described in this paper provide complementary information about deformation in the fault borderlands measured over different time scales. We next interpret each set of observations in the context of the other. The comparison allows us to suggest alternative approaches to future models of GPS data from central California. We also hypothesize that the progressive deformation of some geologic structures in central California is linked to the onset of fault creep along the San Andreas fault.

Geodetic Data Interpreted with Geologic Insight

Our geologic approach, characterizing the style and magnitude of off-fault deformation in the borderlands, provides insight into the interpretation of GPS data across the San Andreas fault. We compare both the map-scale data and the across-fault transects from each data set next, followed by a discussion about the way in which we can incorporate geologic information into future geodetic models for the San Andreas fault in central California.

Comparison of Map Patterns of Deformation

Figure 11 compares geologic evidence for off-fault deformation with the GPS velocity field for the San Andreas fault and its borderlands (and not for the Rinconada fault and the rest of the plate boundary). For the geologic half of the diagram, fold hinges and faults have been colored by basement type, where red tones indicate geologic structures on Salinian basement and blue tones are for those on Franciscan basement.

The geologic structures record very different styles of deformation on either side of the San Andreas fault. Few geologic structures have developed southwest of the fault, except for folds within mostly Pliocene and younger rocks, mostly within 5 km of the fault trace. The majority of structures developed on the Salinian block flank the Rinconada fault on the edge of the map area. In contrast, deformation on Franciscan basement is spread over a broader area, at least 20 km wide, and includes numerous faults and folds. The width of the Franciscan deforming region increases to nearly 40 km adjacent to the creeping segment.

The velocity field also shows evidence for subtle basement control. Two distinct domains are present on Salinian basement, each of which contains domain-consistent velocity vectors in terms of both magnitude and direction. For stations adjacent to the central creeping segment, the GPS residual vectors are south-directed and ~6 mm/yr, whereas those adjacent to the southeast creeping segment are nearly fault-parallel (~30° difference in orientation) and several millimeters per year faster. The internal consistency in these two domains suggests that each is presently translating as a coherent block with little evidence for internal deformation. In contrast, velocity vectors on Franciscan basement change in orientation from nearly fault-parallel to nearly fault-normal from the locked segment toward the creeping segment and also slow down over the same area.

To summarize, the map patterns suggests that basement rocks influence the style of long-term and short-term deformation: Salinian regions have few geologic structures and translate as large blocks, whereas Franciscan regions have more evenly distributed geologic and geodetic deformation.

Comparison of Deformation Rates

An examination of the rates of deformation across the creeping segment (Figs. 10A–10D) also suggests that basement rocks influence the magnitude of deformation. Most of the geologic and geodetic off-fault deformation accrues northeast of the San Andreas fault on Franciscan basement rather than in areas underlain by Salinian basement southwest of the fault.

Geological Society of America Bulletin, published online on 21 January 2011 as doi:10.1130/B30150.1

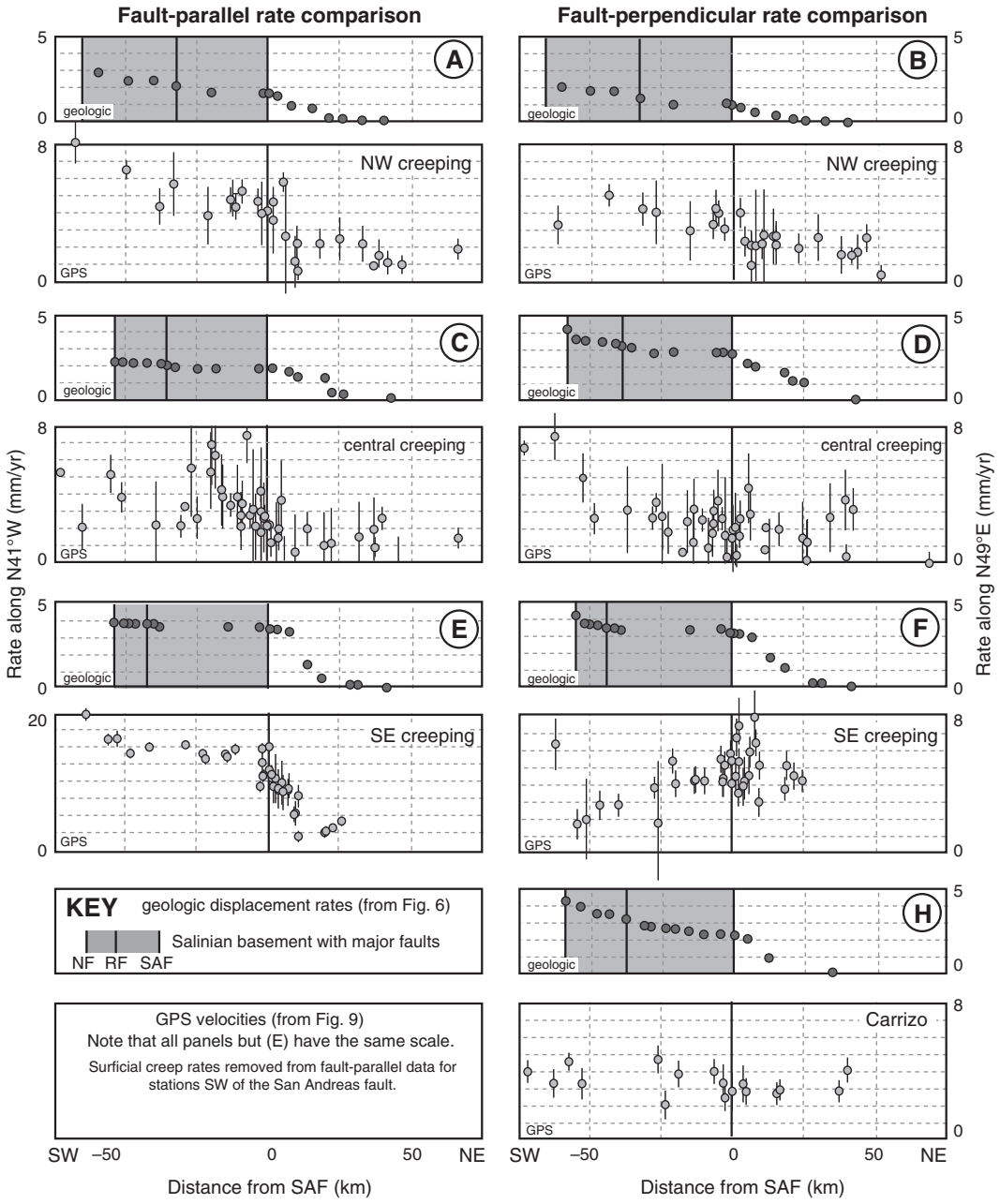

Figure 10. Comparison of deformation gradients from the four transects across central California (data from Figs. 6 and 9). In each pair of panels, the top panel shows geologic displacements as rates assuming that all the deformation occurred in the past 3 m.y. The gray box shows the extent of Salinian basement; the three vertical lines within or bounding the Salinian box are the locations of the Nacimiento (NF), Rinconada (RF), and San Andreas (SAF) faults. The bottom panel shows GPS velocities, where the surficial fault creep rate has been removed for all stations southwest of the fault for the fault-parallel components.

For the borderlands adjacent to the San Andreas fault, we estimate that ~2–3 mm/yr of fault-parallel and fault-perpendicular deformation can be accommodated by off-fault geologic structures, assuming that deformation occurred mostly over the past 3 m.y. For comparison, the geodetic deformation rate for the borderlands (and excluding the fault creep rate) is 3–4 mm/yr, again for both components. Thus, the geologic displacements may account for at least half and possibly all of the off-fault deformation implied by the GPS velocity gradients across the creeping segment.

Implications for Modeling Geodetic Data

The map comparison between geologic and geodetic data suggests that basement rocks with different strengths affect the style of long-term geologic and short-term geodetic deformation (Fig. 11). The transect-based comparison shows that for the creeping segment, where the influence of elastic strain is minimized, similar rates of fault-parallel and fault-perpendicular motion (GPS) and displacements (geologic) are accommodated in the borderlands of the San Andreas fault (Fig. 10).

These observations have potentially important implications for interpretations of geodetic measurements from central California and other locations with one or more major strike-slip faults (Fig. 12). Our results clearly suggest that distributed long-term deformation occurs within the blocks that separate discrete faults in our study area (Fig. 12C). Models of long-term and interseismic motion that ignore this distributed deformation and instead attribute all the deformation to individual discrete faults (Fig. 12A) will either underestimate the cumulative deformation across the region (Fig. 12B) or over-

Geological Society of America Bulletin, published online on 21 January 2011 as doi:10.1130/B30150.1

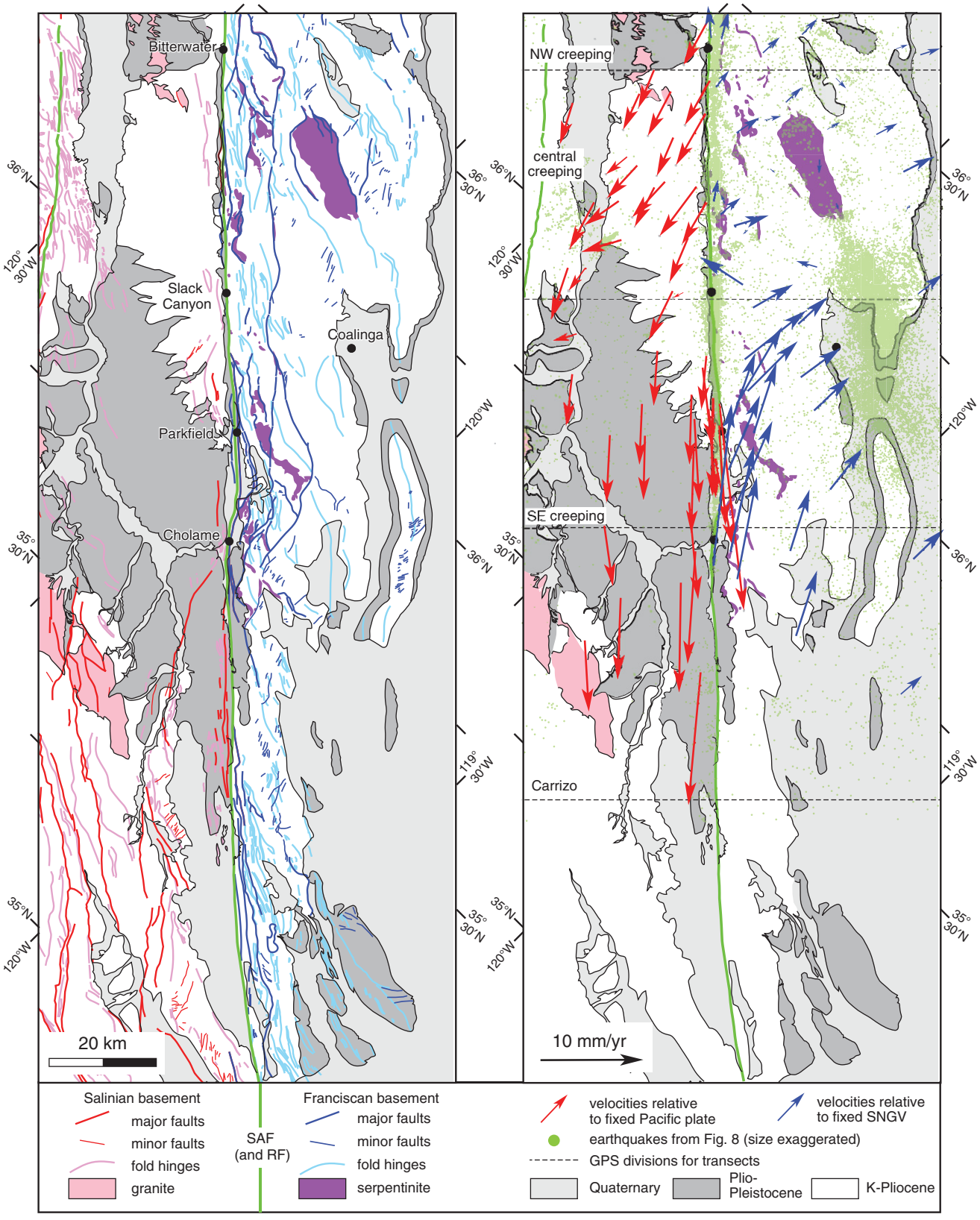

Figure 11. Map comparison of major features of geologic deformation (on left) with major patterns in the GPS velocity field (on right) reproduced from Figure 8. Structures developed on different basement rocks are colored differently (red tones for Salinian block and blue tones for Franciscan block). Details of the comparison are discussed within the text. K—Cretaceous; SNGV—Sierra Nevada–Great Valley.

Geological Society of America Bulletin, published online on 21 January 2011 as doi:10.1130/B30150.1

estimate one or more of the individual fault slip rates if these rates are forced to sum to the total plate motion.

For example, a simple summation of the best estimates for the present slip rates of the San Gregorio–Hosgri fault (3 mm/yr; e.g., WGCEP, 2002), the Rinconada fault (1 mm/yr; Rolandone et al., 2008; Bird, 2009), and the present creep rate for the San Andreas fault (28–30 mm/yr; Titus et al., 2006) give a summed slip rate of 32–34 mm/yr (Fig. 12B), which is 3–5 mm/yr slower than our own GPS-based estimates for Sierra Nevada–Great Valley–Pacific plate motion in central California (shaded line in Fig. 12B) and 4–7 mm/yr slower than previous geodetic estimates (Argus and Gordon, 2001; d'Alessio et al., 2005). One way to reconcile the difference between the summed fault slip rates and fault-parallel component of plate motion is to assume that partial locking at depth of the creeping segment of the San Andreas fault causes distributed elastic (interseismic) deformation in the fault borderlands. Doing so implies a long-term fault slip rate of ~33–35 mm/yr.

Although our GPS observations are too noisy to exclude the hypothesis that partial locking of the central creeping segment is the cause of gradients in fault-parallel velocities adjacent to the San Andreas fault, our geologic analysis suggests that the borderlands accommodate as much permanent fault-parallel deformation as they do fault-perpendicular deformation (Figs. 12C–12D). By implication, active deformation in the borderlands, rather than deep locking of the creeping segment of the San Andreas fault, causes the observed GPS velocity gradients. With this view, the fault-parallel plate motion rate can be met without assuming that elastic strain is accumulating on the San Andreas fault (Fig. 12D).

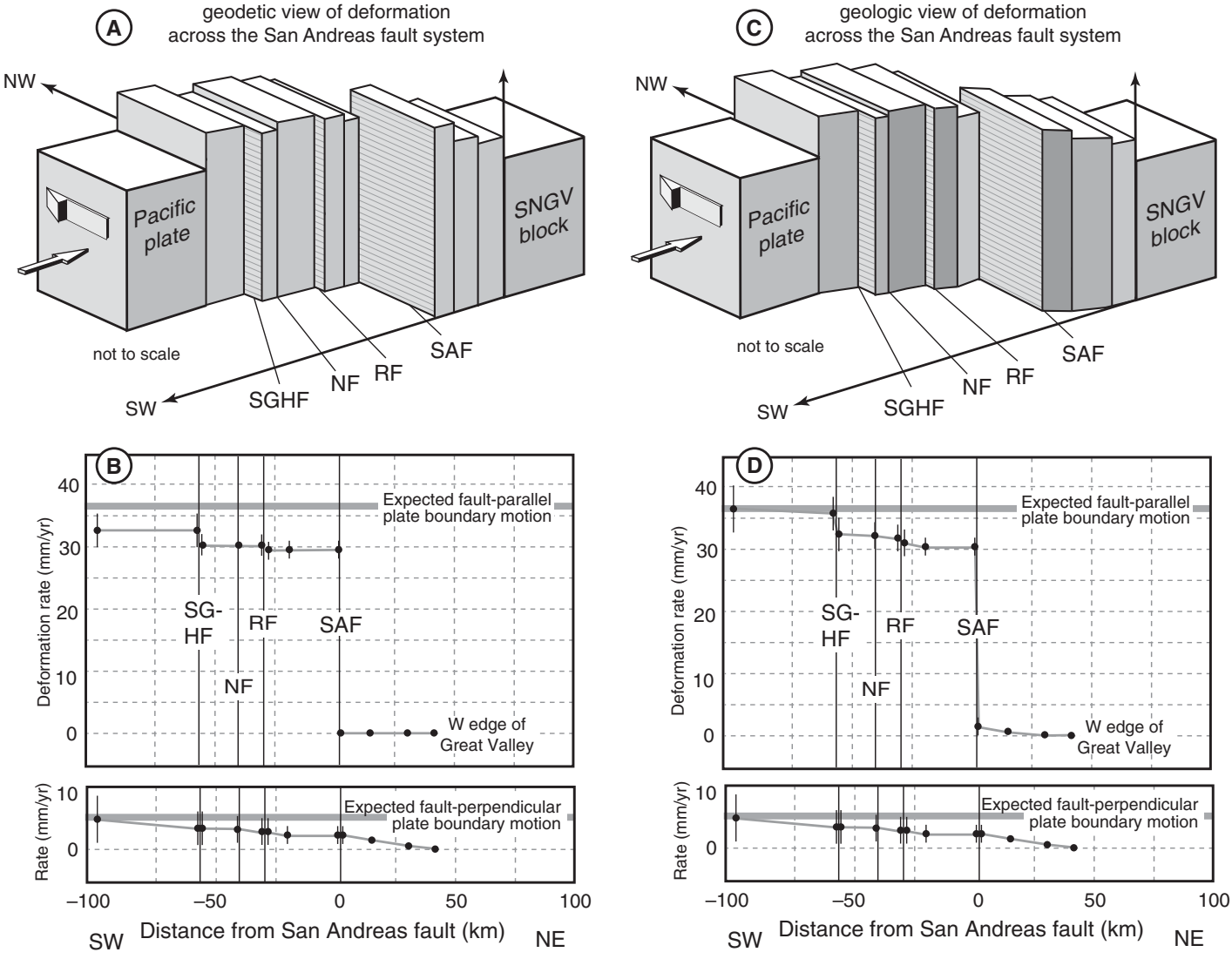

Figure 12. Two ways to view plate boundary deformation in central California: the classic geodetic view (left column) versus our geologic view (right column), which more explicitly accounts for permanent deformation. The top diagram in each column is a cartoon block diagram of the major faults and borderland blocks in central California. The two graphs beneath each block diagram summarize the fault-parallel and fault-perpendicular contributions of deformation from these two views of deformation across the plate boundary system. SNGV—Sierra Nevada–Great Valley. Faults are abbreviated as: SGHF—San Gregorio–Hosgri, NF—Nacimiento, RF—Rinconada, and SAF—San Andreas.

Geological Society of America Bulletin, published online on 21 January 2011 as doi:10.1130/B30150.1

If we extrapolate the fault-perpendicular deformation rate that we estimate from Franciscan basement northeast of the San Andreas fault (i.e., ~2 mm/yr for a 40-km-wide region) to the southwest across the plate boundary to Franciscan basement west of the Nacimiento fault (lower panel of Fig. 12D), the extrapolated geologic rate is the same within uncertainties as the fault-perpendicular rate estimated with our Sierra Nevada–Great Valley–Pacific angular velocity (5.4 ± 0.3 mm/yr). Previous authors (e.g., Argus and Gordon, 2001) correctly attribute the ~3–5 mm/yr fault-perpendicular component of plate motion in central California to permanent off-fault deformation and excluded this component from elastic models (e.g., Rolandone et al., 2008). By analogy, we suggest that future models of deformation in this region must allow for a comparable amount of fault-parallel distributed deformation.

A reexamination of slip rates along the San Andreas fault in central California, in light of the style of permanent geologic deformation, suggests that the 31–35 mm/yr slip rate for the creeping segment estimated by Rolandone et al. (2008) may be too fast by as much as 3 mm/yr. If similar downward adjustments apply to the Parkfield and Carrizo segments, for which deep slip rate estimates are typically 33–36 mm/yr (Harris and Segall, 1987; King et al., 1987; Lisowski et al., 1991; Murray et al., 2001; Schmalzle et al., 2006), then the revised slip rates would be 30–33 mm/yr. The slower range of rates is consistent with a 31.5 mm/yr rate estimated by Bird (2009) from a model that includes distributed deformation. These slower fault slip rates are also compatible with the often-cited 34 ± 3 mm/yr Holocene slip rate from the Carrizo plain (Sieh and Jahns, 1984) and are consistent with the 29.3–35.6 mm/yr range of slip rates estimated by Noriega et al. (2006) from multiple fault trenches in the Carrizo plain.

Taken together, the 28–30 mm/yr surficial creep rate measured along the central creeping segment (Titus et al., 2006) and 29–36 mm/yr range of paleoseismologic estimates for the long-term slip rate in the Carrizo plain are consistent with a long-term slip rate along the San Andreas fault in central California of 30 ± 2 mm/yr.

Geologic Data Interpreted with Geodetic Insight

We next use the well-defined pattern of dilatation determined from our GPS velocity field and strain modeling as a basis for interpreting recent geologic deformation (Fig. 13). In particular, we propose a two-stage kinematic model that links the onset of fault creep to the growth of particular geologic structures, including folds of the Coalinga and Kettleman Hills anticlines (Fig. 14).

Comparison of Mapped Patterns of Deformation

Figure 13 compares dilatational strain rates derived from modeling of the GPS velocity field with independent indicators of recent geologic deformation adjacent to the San Andreas fault, including folds in Pliocene and younger sedimentary rocks, recent earthquakes, and detailed outlines of Quaternary alluvial systems throughout the region. The region of significant contractional strain northeast of the San Andreas fault derived from our GPS velocities overlaps the actively growing Coalinga and Kettleman Hills anticlines, where numerous earthquakes associated with thrust faulting occur. Southwest of the fault, the region of extensional dilatation strain rate derived from GPS observations coincides with a virtually undeformed stretch of flat-lying sedimentary rocks on Salinian basement.

As described in the strain modeling section, our simple elastic model that incorporates a gradual transition from locked to creeping behavior (Figs. 7B–7C; Rolandone et al., 2008) matches the large-scale patterns in the GPS velocity field. In particular, the model predicts the rapid fault-parallel motions for GPS sites along the SE creeping and Carrizo segments as well as the slower more fault-normal motions along the central creeping segment. The obvious geographic overlap of the prominent contractional structures northeast of the fault and the region of interseismic contractional strain emphasized in Figure 13 clearly suggests that over many earthquake cycles, geologic structures in the fault borderlands relieve some of the interseismic elastic strain that accumulates in the borderlands. Earthquakes on adjoining locked or partly locked segments of the San Andreas fault relieve the remainder of the strain via coseismic elastic strain release. Moreover, major along-strike variations in the fault locking (i.e., the transition from a fully locked fault to a creeping fault) and variations in basement rheology (e.g., Schmalzle et al., 2006) may strongly influence the location of accumulating off-fault deformation, as emphasized next.

Implications for the Development of Geologic Structures in Central California

We present a new conceptual model for the development of geologic structures over the past 8 m.y. in central California that integrates information from the map-based comparisons, including the different strengths of basement rocks in the region (Fig. 11) and the strain rate patterns adjacent to creeping and locked segments of the San Andreas fault (Fig. 13). In particular, the model seeks to explain the present orientations of the Coalinga and Kettleman Hills anticlines. These folds, which are located within the contractional strain region north of Parkfield (Fig. 13), are difficult to interpret using our simple kinematic model of fold development. Their hinge orientations and limb dips suggest that both folds formed in their present orientation (Fig. 3B; with an angle of oblique convergence of 80°–90°), consistent with borehole breakouts (Zoback et al., 1987; Townend and Zoback, 2004), earthquake focal mechanisms (Eaton, 1990), and the GPS velocity field (Fig. 8). However, paleomagnetic data (White, 1987; Tetreault, 2006), hinge-perpendicular normal faults (Woodring et al., 1940), and the en echelon fold hinge geometry (Miller, 1998) demonstrate that these folds must have rotated during fold growth.

Miller (1998) reconciled these seemingly incompatible observations by suggesting that these folds grew under changing kinematic conditions with an increased magnitude of shortening (that facilitated rapid rotation) over time. He proposed that the kinematic change was related to the shift in relative plate motion from oblique divergence to oblique convergence. However, because more recent estimates have pushed the age of transpression to ca. 8 Ma (Atwater and Stock, 1998), this plate motion shift no longer coincides with the rapid growth of these anticlines over the past 2–2.5 m.y. (Wentworth and Zoback, 1989).

We instead suggest that the changing kinematic conditions imposed on these anticlines may be linked to the onset of fault creep in central California, illustrated by a series of time steps in Figure 14. We hypothesize that folding initiated adjacent to a locked San Andreas fault, perhaps as early as 8 Ma when the relative plate motion changed. If velocity vectors at ca. 8 Ma were similar to those presently observed adjacent to the Carrizo segment (Fig. 14A), the velocity field would have promoted deformation of the Franciscan basement everywhere northeast of the locked San Andreas fault, creating a series of en echelon folds oblique to the fault strike (Fig. 14B) that were envisioned in the early models for wrench folding (Wilcox et al., 1973; Harding, 1976, 1988). Limited deformation may have occurred in the less deformable sedimentary rocks on Salinian basement, but the granites presently exposed between Salinas and Soledad may have been adjacent to this segment of the fault at 5 Ma (Fig. 14B), effectively prohibiting deformation. Once fault creep began on the San Andreas fault, we hypothesize that the paleo–velocity field was altered into a form analogous with the present interseismic

Geological Society of America Bulletin, published online on 21 January 2011 as doi:10.1130/B30150.1

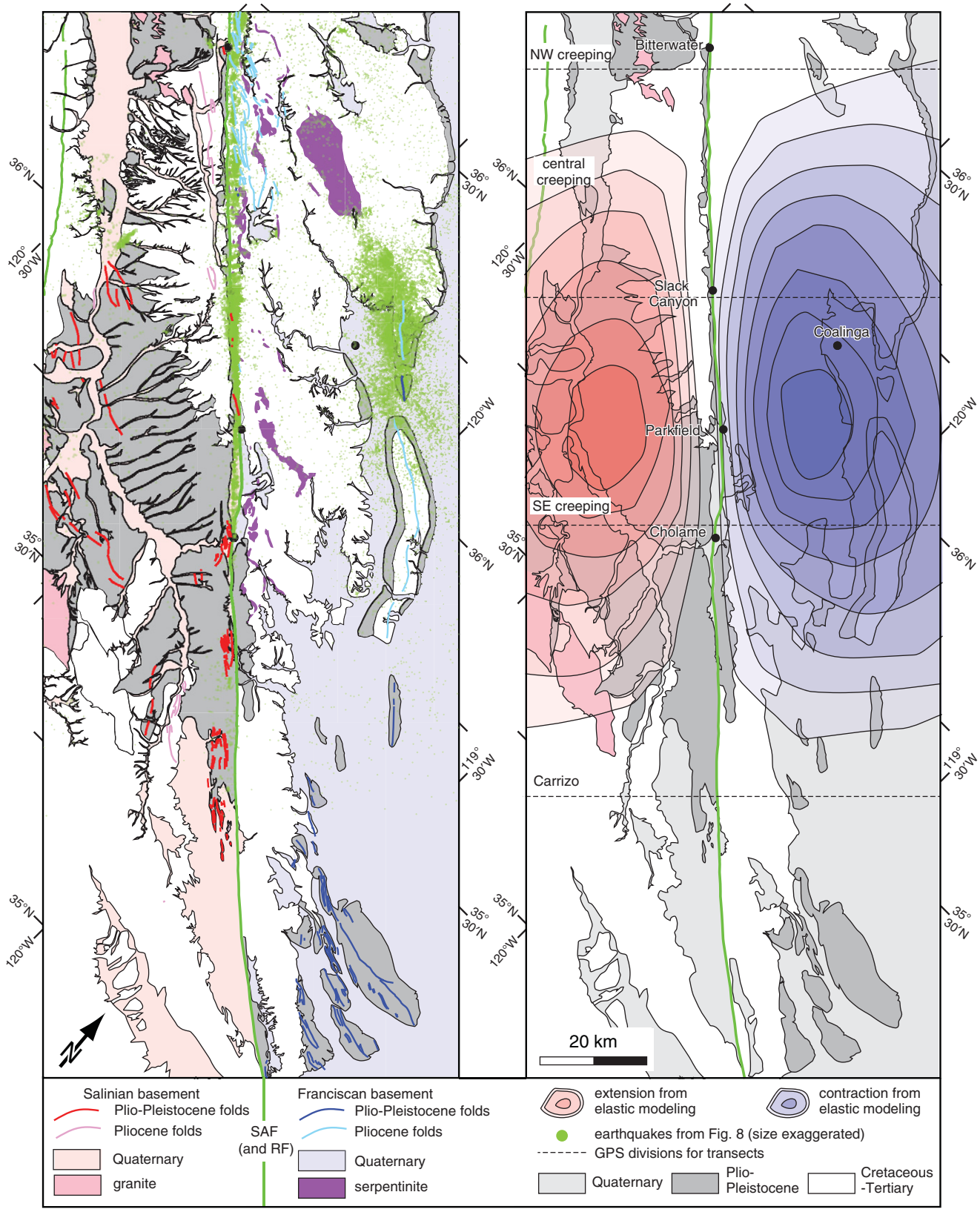

Figure 13. Map comparison of recent features of geologic deformation (on left) with dilatation regions from the elastic modeling (on right) reproduced from Figure 10C. Note the overlap of the contractional region with the Coalinga and Kettleman Hills anticlines (and their associated seismicity). The extensional region overlaps the large Pliocene–Pleistocene Paso Robles Formation basin, where Quaternary drainage channels are evenly spaced and parallel, and where there is a distinct orientation relative to other drainage systems in the region.

Geological Society of America Bulletin, published online on 21 January 2011 as doi:10.1130/B30150.1

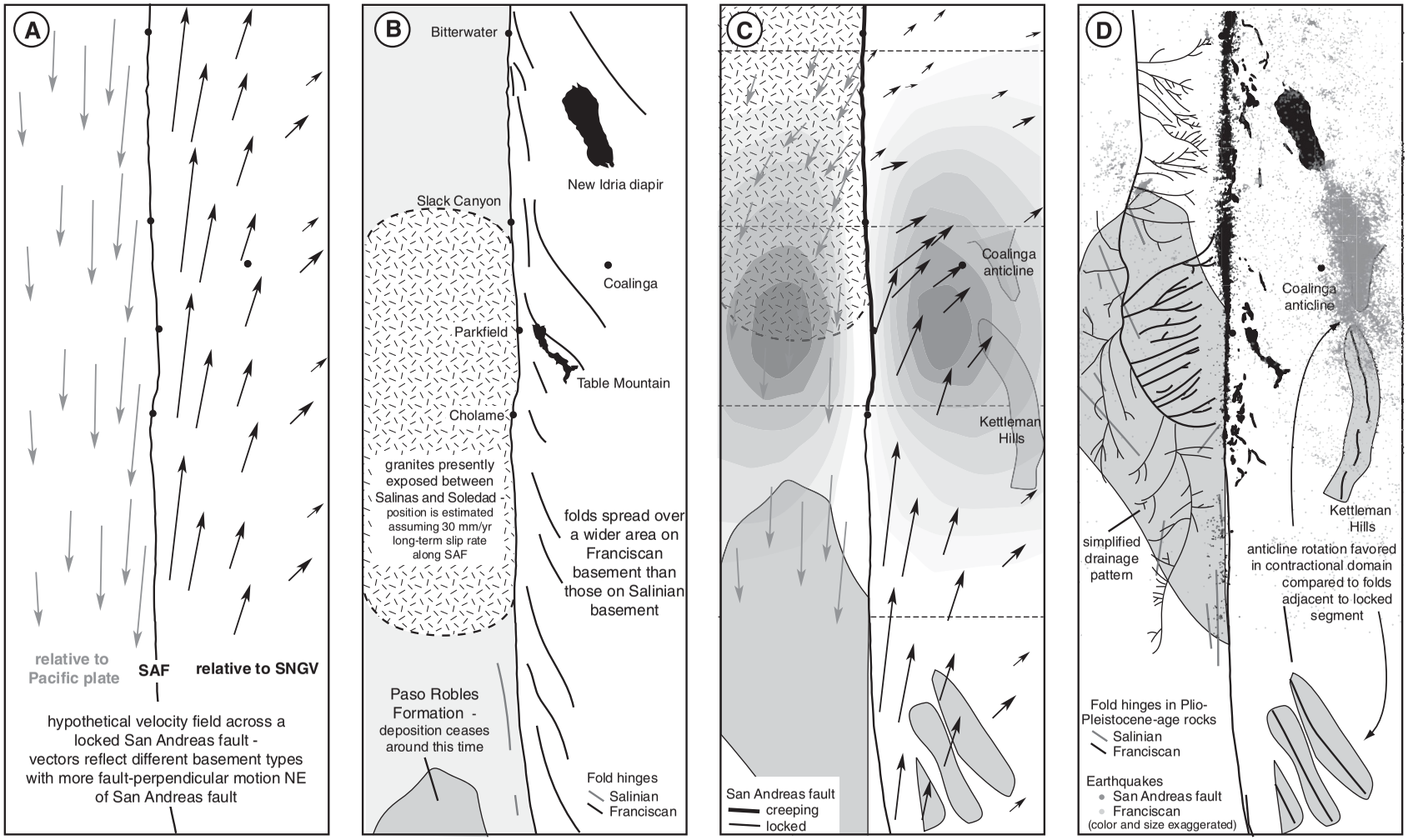

Figure 14. Schematic diagram illustrating the proposed tectonic development of regional geologic structures. The Franciscan side has been fixed in this diagram; blocks southwest of the fault are assumed to move at the average long-term slip rate of ~30 mm/yr. This rate requires more offset than the 25 km suggested by Galehouse (1967) for the Paso Robles Formation basin. (A) The hypothetical paleo–velocity field for a locked fault throughout central California. Note that velocity vectors northeast of the San Andreas fault have a larger fault-perpendicular component because the velocity field is affected by the weaker Franciscan rocks. (B) The geologic response to this velocity field, which causes en echelon folds to develop on Franciscan basement and little deformation on Salinian basement. The folds in this panel have been simplified from the actual fold patterns (compare with Fig. 2). With the onset of fault creep along the San Andreas fault (C), the hypothesized paleo–velocity field changes orientation and magnitude near the creeping segment, causing the two dilatational regions on either side of the transition from creeping to locked behavior. (D) Overlap of the contractional region with the Coalinga and Kettleman Hills anticlines, the orientations of which are anomalous. Recent seismicity due to the New Idria, Coalinga, and Kettleman Hills earthquakes all fall within the predicted region of contraction. The extensional region coincides with Quaternary drainage channels that have a distinct orientation relative to other systems in central California (see also Fig. 13). These simplified data (D) also show the spatial correlation between microseismicity defining creeping behavior along the San Andreas fault and exposures of serpentinite in the Franciscan block.

Geological Society of America Bulletin, published online on 21 January 2011 as doi:10.1130/B30150.1

velocity field (Fig. 14C). This change would have promoted broad regions of extension and contraction in the borderlands corresponding to the transitions from creeping to locked behavior. The pattern of paleostrain during this phase may have promoted fold growth and rotation of the Coalinga and Kettleman Hills anticlines into their present fault-parallel orientations. In contrast, the folds in Pliocene–Pleistocene rocks adjacent to the Carrizo segment, where the pattern of paleostrain remained the same, maintained their en echelon geometry (Fig. 14D).

The onset of fault creep in central California also may have influenced the development of geologic structures southwest of the San Andreas fault. This correlation is much more speculative, however, because the predicted extension (Fig. 14C) would have occurred within the Salinian block, which is less likely to deform than Franciscan rocks over geologic and geodetic time scales (Fig. 10). The most compelling evidence for extension is, in some sense, the absence of the expected plate boundary transpression. Gentle folds, with limb dips often less than 10°, have localized in the Paso Robles Formation on the edges of the extensional region (Fig. 14D). The Quaternary drainage pattern is also distinct in this area, with evenly spaced, parallel channels containing fewer branching patterns than anywhere else in the region (highlighted in pink in Fig. 14D). The channel system in older sedimentary rocks adjacent to the central creeping segment has a different orientation and a more fully developed dendritic drainage pattern. It is possible that the channel orientations within the extensional region are fault-controlled, or perhaps their consistent orientation reflects a gentle tilting of Tertiary sediments toward the extension region. To summarize, little geologic deformation has occurred within the extensional region, whereas folds are found on its fringes. Whether or not this relates to the predicted extension is difficult to determine without much more careful field observations.

Timing estimates for the growth of regional structures are broadly consistent with our hypothesis that fault creep has influenced the development of off-fault structures. Northeast of the San Andreas fault, folds close to the fault are mostly older than those on the edge of the Great Valley. The Vallecitos syncline began in the Paleocene or Eocene as a sedimentary basin (Harding, 1976; Page et al., 1998), with some fold growth in the Miocene (Enos, 1961) followed by post-Pliocene refolding within the basin (Wilkinson, 1960). In contrast, the Kettleman Hills North Dome and Coalinga anticlines underwent their primary growth in the past 2–2.5 m.y. (Wentworth and Zoback, 1989; Bloch et al., 1993; Page et al., 1998). The Paso Robles Formation southwest of the fault is typically mapped as Pliocene–Pleistocene in age (e.g., Dibblee, 1971, 1972), but Galehouse (1967) argued that it is Pliocene based on fossil evidence. This suggests that deposition ceased by ~5 m.y. in response to plate boundary transpression and uplift of the Coast Ranges (Fig. 14B), suggesting that fault creep could not yet have been occurring in the area.

Aseismic creep rates along much of the creeping segment have remained steady for at least the past 35 yr (Titus et al., 2006), and several lines of evidence suggest that creep has been an important deformation style for longer periods of time. Fences offset by the fault representing 100-yr time scales have rates consistent with modern measures (Hay et al., 1989). Trenching near the central creeping segment found a long-term rate of 28 mm/yr for the past ~1000 yr (Cotton et al., 1986). Different microstructures have developed in trenches across creeping and noncreeping sections of the fault, with radiocarbon dates suggesting creeping behavior for >1000 yr (Cashman et al., 2007). Heat-flow patterns across the fault are consistent with models that assume a creeping fault for the past 5 m.y. (d'Alessio et al., 2006). Last, the strong correlation between serpentinite exposures northeast of the San Andreas fault and microseismicity defining the creeping segment suggest that fault creep is ultimately linked to these Franciscan rocks (Fig. 14D). The presence of talc in the SAFOD drill hole, which is one explanation of the actual mechanism facilitating fault creep (Moore and Rymer, 2007), could be the result of rehydrated serpentinites. The two largest serpentinite bodies—New Idria and Table Mountain—are believed to have been at the surface for millions of years. Clasts of sedimentary serpentine in the mid-Miocene Big Blue Formation (Casey and Dickinson, 1976), which forms part of the east limb of the Coalinga anticline, are believed to have come from New Idria. Dickinson (1966) estimated that Table Mountain (Fig. 14B) was forcefully extruded in Pliocene–Pleistocene times. Thus, the serpentinites that promote fault creep were at the surface, and were presumably sufficiently distributed along the upper-crustal portion of the fault zone to cause fault creep along part of the San Andreas fault by the Pliocene, thereby altering the paleo–velocity field (Fig. 14C).

Our hypothesis suggests that the style of off-fault deformation was fundamentally altered when creeping behavior began along the San Andreas fault and that several enigmatic geologic structures reflect the new kinematic conditions resulting from fault creep. The Coalinga and Kettleman Hills anticlines provide our best estimate on the timing of this event because these structures formed in contraction, not extension, where timing evidence would tend to be buried. Further, the folds are on the Franciscan side of the plate boundary, which likely remained fixed relative to the creeping segment since fault creep is probably tied to Franciscan serpentinites. Based on the major phase of growth for these two anticlines (Wentworth and Zoback, 1989), we suggest that the creeping segment may have experienced aseismic creep for the past 2–2.5 m.y.

CONCLUSIONS

We compare the styles and magnitudes of geologic and geodetic deformation in the borderlands adjacent to the San Andreas fault system in central California. Our geologic analysis demonstrates that off-fault structures not only record the fault-perpendicular displacements recognized by many workers (e.g., Mount and Suppe, 1987; Zoback et al., 1987; Namson and Davis, 1988), but they also record significant, comparable fault-parallel displacements less frequently recognized in the literature (see, however, Jamison, 1991; Miller, 1998; Teyssier and Tikoff, 1998; Titus et al., 2007). GPS velocity gradients demonstrate that both fault-perpendicular and fault-parallel motion is accommodated away from the major strike-slip faults between the Pacific plate and Sierra Nevada–Great Valley block. Strain rates and strain axis orientations from the GPS velocity field reveal a regional pattern of contraction and extension predicted by a simple elastic model that incorporates the change from locked to creeping behavior along the San Andreas fault.

The geologic and geodetic observations from central California provide a clearer picture of the partitioning of plate boundary deformation. Most importantly, off-fault permanent deformation may accommodate up to 10% of the modern fault-parallel plate motion. The synthesis of these two data sets also provides insight into plate boundary deformation that would be difficult to extract from either data set alone. Geologic insight improves our geodetic interpretations by demonstrating that basement rocks control the distribution of deformation. Further, because geodetic and geologic patterns of deformation from the borderlands are generally consistent, some of the short-term strain that is typically considered to be relieved by occasional earthquakes and accelerated afterslip along the San Andreas fault instead results in permanent off-fault deformation in the borderlands. Consequently, elastic models of the modern velocity gradient across the San

Andreas fault that ignore off-fault deformation will overestimate the long-term fault slip rate on the few major faults that are modeled. Geodetic insight improves our geologic interpretations by providing a clearer picture of the kinematic consequences of the change from locked to creeping behavior along the San Andreas fault. The histories of the Coalinga and Kettleman Hills anticlines cannot be explained by a single kinematic episode, since their present orientations and limb dips suggest that they initiated parallel to the San Andreas fault, but these same folds have rotated 10°–24° based on paleomagnetic data. Instead, their histories can be better explained due to a shift from a locked San Andreas fault to an aseismic fault in central California. Thus, the transition from a locked fault to a creeping fault in space and also in time plays an important role in the development of regional geologic structures.

ACKNOWLEDGMENTS

We thank Joshua Davis, Scott Giorgis, Zack McGuire, Skylar Primm, Paul Riley, and Bill Titus for their sweaty assistance collecting campaign GPS data. We also thank Joshua Davis for code used to compute useful strain parameters. Eric Horsman is thanked for innumerable conversations about the ideas in the manuscript and suggestions on earlier drafts. We thank Susanne Janecke for comments on an early version of the manuscript and John Fletcher, Mike Oskin, and Rocco Malservisi for comments and suggestions that helped us better clarify the ideas within the manuscript. We gratefully acknowledge the numerous landowners in central California who allowed access to key locations, especially the assistance of Phil Martin, Bill Petrovich, and Bill Whitney. This material is based on work supported under a National Science Foundation Graduate Research Fellowship (Titus), an Allensworth fellowship from the Department of Geology at Carleton College (Dyson), and by National Science Foundation grants EAR-0208038 (DeMets and Tikoff) and EAR-0337308 (Bürgmann).

REFERENCES CITED

Allen, C.R., 1968, The tectonic environments of seismically active and inactive areas along the San Andreas fault system: Stanford University Publications in Geological Sciences, v. 11, p. 70–80.

Allmendinger, R.W., 1998, Inverse and forward numerical modeling of trishear fault-propagation folds: Tectonics, v. 17, p. 640–656, doi: 10.1029/98TC01907.

Allmendinger, R.W., Reilinger, R., and Loveless, J., 2007, Strain and rotation rate from GPS in Tibet, Anatolia, and the Altiplano: Tectonics, v. 26, doi: 10.1029/2006TC002030.

Altamimi, Z., Collilieux, X., Legrand, J., Garayt, B., and Boucher, C., 2007, ITRF2005; a new release of the International Terrestrial Reference Frame based on time series of station positions and Earth orientation parameters: Journal of Geophysical Research, v. 112, p. B09401, doi: 10.1029/2007JB004949.

Argus, D.F., and Gordon, R.G., 2001, Present tectonic motion across the Coast Ranges and San Andreas fault system in central California: Geological Society of America Bulletin, v. 113, p. 1580–1592, doi: 10.1130/0016-7606(2001)113<1580:PTMATC>2.0.CO;2.

Atwater, T., 1970, Implications of plate tectonics for the Cenozoic tectonic evolution of western North America: Geological Society of America Bulletin, v. 81, p. 3513–3535, doi: 10.1130/0016-7606(1970)81[3513:IOPTFT]2.0.CO;2.

Atwater, T., and Stock, J., 1998, Pacific–North America plate tectonics of the Neogene southwestern United States; an update: International Geology Review, v. 40, p. 375–402, doi: 10.1080/00206819809465216.

Bartow, J.A., 1991, The Cenozoic Evolution of the San Joaquin Valley, California: U.S. Geological Survey Professional Paper 1501, 40 p.

Bilham, R., and Bodin, P., 1992, Fault zone connectivity; slip rates on faults in the San Francisco Bay area, California: Science, v. 258, p. 281–284, doi: 10.1126/science.258.5080.281.

Bird, P., 2009, Long-term fault slip rates, distributed deformation rates, and forecast of seismicity in the western United States from joint fitting of community geologic, geodetic, and stress direction data sets: Journal of Geophysical Research, v. 114, doi: 10.1029/2009JB006317.

Blake, M.C., Jr., Campbell, R.H., Dibblee, T.W., Jr., Howell, D.G., Nilsen, T.H., Normark, W.R., Vedder, J.G., and Silver, E.A., 1978, Neogene basin formation in relation to plate tectonic evolution of San Andreas fault system, California: The American Association of Petroleum Geologists Bulletin, v. 62, p. 344–372.

Blewitt, G., 2008, Fixed point theorems of GPS carrier phase ambiguity resolution and their application to massive network processing: Ambizap: Journal of Geophysical Research, v. 113, p. B12410, doi: 10.1029/2008JB005736.

Bloch, R.B., von Huene, R., Hart, P.E., and Wentworth, C.M., 1993, Style and magnitude of tectonic shortening normal to the San Andreas fault across Pyramid Hills and Kettleman Hills South Dome, California: Geological Society of America Bulletin, v. 105, p. 464–478, doi: 10.1130/0016-7606(1993)105<0464:SAMOTS>2.3.CO;2.

Burford, R.O., 1988, Retardations in fault creep rates before local moderate earthquakes along the San Andreas fault system, central California: Pure and Applied Geophysics, v. 126, p. 499–529, doi: 10.1007/BF00879008.

Burford, R.O., and Harsh, P.W., 1980, Slip on the San Andreas fault in central California from alignment array surveys: Bulletin of the Seismological Society of America, v. 70, p. 1233–1261.

Bürgmann, R., 1991, Transpression along the southern San Andreas fault, Durmid Hill, California: Tectonics, v. 10, p. 1152–1163, doi: 10.1029/91TC01443.

Byerly, P.E., 1966, Interpretations of gravity data from the central Coast Ranges and San Joaquin Valley, California: Geological Society of America Bulletin, v. 77, p. 83–94, doi: 10.1130/0016-7606(1966)77[83:IOGDFT]2.0.CO;2.

Casey, T.A.L., and Dickinson, W.R., 1976, Sedimentary serpentinite of the Miocene Big Blue Formation near Cantua Creek, California: AAPG-SEPM-SEG Pacific Sections meeting, v. 60, p. 2177.

Cashman, S.M., Baldwin, J.N., Cashman, K.V., Swanson, K., and Crawford, R., 2007, Microstructures developed by coseismic and aseismic faulting in near-surface sediments, San Andreas fault, California: Geology, v. 35, p. 611–614, doi: 10.1130/G23545A.1.

Chester, J.S., and Chester, F.M., 1990, Fault-propagation folds above thrusts with constant dip: Journal of Structural Geology, v. 12, p. 903–910, doi: 10.1016/0191-8141(90)90063-5.

Christensen, M.N., 1965, Late Cenozoic deformation in the central Coast Ranges of California: Geological Society of America Bulletin, v. 76, p. 1105–1124, doi: 10.1130/0016-7606(1965)76[1105:LCDITC]2.0.CO;2.

Clark, J.C., 1998, Neotectonics of the San Gregorio fault zone; age dating controls on offset history and slip rates: The American Association of Petroleum Geologists Bulletin, v. 82, p. 844–845.

Compton, R.R., 1966, Analyses of Pliocene–Pleistocene deformation and stresses in northern Santa Lucia Range, California: Geological Society of America Bulletin, v. 77, p. 1361–1379, doi: 10.1130/0016-7606(1966)77[1361:AOPDAS]2.0.CO;2.

Cotton, W.R., Hall, N.T., and Hay, E.A., 1986, Holocene Behavior of the Hayward-Calaveras Fault System, San Francisco Bay Area, California: U.S. Geological Survey Contract 14–08–0001–20555, 15 p.

Cox, A., and Engebretson, D.C., 1985, Change in motion of Pacific plate at 5 Myr BP: Nature, v. 313, p. 472–474, doi: 10.1038/313472a0.

Crump, S., Titus, S.J., McGuire, Z., and Housen, B., 2009, Paleomagnetic data from the Rinconada fault in central California: Evidence for off-fault deformation: Eos (Transactions, American Geophysical Union), v. 90, no. 52, Fall Meeting supplement, abstract G33B–0650.

Dahlstrom, C.D.A., 1990, Geometric constraints derived from the law of conservation of volume and applied to evolutionary models for detachment folding: The American Association of Petroleum Geologists Bulletin, v. 74, p. 336–344.

d'Alessio, M.A., Johanson, I.A., Bürgmann, R., Schmidt, D.A., and Murray, M.H., 2005, Slicing up the San Francisco Bay area; block kinematics and fault slip rates from GPS-derived surface velocities: Journal of Geophysical Research, v. 110, p. B06403, doi: 10.1029/2004JB003496.

d'Alessio, M.A., Williams, C.F., and Bürgmann, R., 2006, Frictional strength heterogeneity and surface heat flow; implications for the strength of the creeping San Andreas fault: Journal of Geophysical Research, v. 111, p. B05410, doi: 10.1029/2005JB003780.

Dewey, J.F., 2002, Transtension in arcs and orogens: International Geology Review, v. 44, p. 402–439, doi: 10.2747/0020-6814.44.5.402.

Dibblee, T.W., Jr., 1971, Geologic Maps of Seventeen 15-Minute Quadrangles along the San Andreas Fault in Vicinity of King City, Coalinga, Panoche Valley, and Paso Robles, California: U.S. Geological Society Open-File Report 71–87, scale 1:62,500.

Dibblee, T.W., Jr., 1972, Geologic Maps of Fourteen 15-Minute Quadrangles along the San Andreas Fault in the Vicinity of Paso Robles and Cholame Southeastward to Maricopa and Cuyama, California: U.S. Geological Society Open-File Report 72–89, scale 1:62,500.

Dibblee, T.W., Jr., 1975, Geologic Maps of the Pacheco Pass, Hollister, Quien Sabe, Ortigalita Peak, San Benito, Panoche Valley, and "Tumey Hills" Quadrangles; San Benito, Santa Clara, Merced, and Fresno Counties, California: U.S. Geological Society Open-File Report 75–394, scale 1:62,500.

Dibblee, T.W., Jr., 1976, The Rinconada and related faults in the southern Coast Ranges, California, and their tectonic significance, U. S. Geological Survey Professional Paper 981, 55 p.

Dibblee, T.W., Jr., Graham, S.E., Mahony, T.M., Blissenbach, J.L., Mariant, J.J., and Wentworth, C.M., 1999, Regional geologic Map of San Andreas and Related Faults in Carrizo Plain, Temblor, Caliente and La Panza Ranges and Vicinity, California; a Digital Database: U.S. Geological Survey Open-File 99–0014, scale 1:125,000.

Dibblee Foundation, assorted years, DF206 Caldwell Mesa, DF210 Tar Spring Ridge, DF211 Arroyo Grande NE, DF215 Morro Bay North, DF363 Lopez Point, DF365 Pebblestone, DF368 Alder Peak, scale 1:24,000.

Dickinson, W.R., 1966, Table Mountain serpentinite extrusion in California Coast Ranges: Geological Society of America Bulletin, v. 77, p. 451–472, doi: 10.1130/0016-7606(1966)77[451:TMSEIC]2.0.CO;2.

Dickinson, W.R., 1983, Cretaceous sinistral strike slip along Nacimiento fault in coastal California: The American Association of Petroleum Geologists Bulletin, v. 67, p. 624–645.

Dickinson, W.R., 1997, Tectonic implications of Cenozoic volcanism in coastal California: Geological Society of America Bulletin, v. 109, p. 936–954, doi: 10.1130/0016-7606(1997)109<0936:OTIOCV>2.3.CO;2.

Dickinson, W.R., and Rich, E.I., 1972, Petrologic intervals and petrofacies in the Great Valley Sequence, Sacramento Valley, California: Geological Society of America Bulletin, v. 83, p. 3007–3024, doi: 10.1130/0016-7606(1972)83[3007:PIAPIT]2.0.CO;2.

Dickinson, W.R., Ducea, M., Rosenberg, L.I., Greene, H.G., Graham, S.A., Clark, J.C., Weber, G.E., Kidder, S., Ernst, G.W., and Brabb, E.E., 2005, Net dextral slip, Neogene San Gregorio–Hosgri fault zone, coastal California; geologic evidence and tectonic implications, *in* Geological Society of America Special Paper 391, 43 p.

Dixon, T.H., Miller, M., Farina, F., Wang, H., and Johnson, D., 2000, Present-day motion of the Sierra Nevada block and some tectonic implications for the Basin and Range Province, North American Cordillera: Tectonics, v. 19, p. 1–24, doi: 10.1029/1998TC001088.

Ducea, M., House, M.A., and Kidder, S., 2003, Late Cenozoic denudation and uplift rates in the Santa Lucia Mountains, California: Geology, v. 31, p. 139–142, doi: 10.1130/0091-7613(2003)031<0139:LCDAUR>2.0.CO;2.

Eaton, J.P., 1990, The earthquake and its aftershocks from May 2 through September 30, 1983, *in* Rymer, M.J., and Ellsworth, W.L., eds., The Coalinga, California Earthquake of May 2, 1983: U.S. Geological Survey Professional Paper 1487, p. 113–170.

Ekström, G., Stein, R.S., Eaton, J.P., and Eberhart-Phillips, D., 1992, Seismicity and geometry of a 110-km-long blind thrust fault: 1. The 1985 Kettleman Hills, California, earthquake: Journal of Geophysical Research, v. 97, p. 4843–4864, doi: 10.1029/91JB02925.

Enos, P.P., 1961, Geologic Problems in the Western Vallecitos Syncline, San Benito County, California [Master's thesis]: Stanford, Stanford University, 90 p.

Ernst, G.W., 1981, Summary of the geotectonic development of California, *in* Ernst, G.W., ed., The geotectonic development of California; Rubey Volume 1: Englewood Cliffs, New Jersey, Prentice-Hall, p. 601–613.

Erslev, E.A., 1991, Trishear fault-propagation folding: Geology, v. 19, p. 617–620, doi: 10.1130/0091-7613(1991)019<0617:TFPF>2.3.CO;2.

Flinn, D., 1979, The deformation matrix and the deformation ellipsoid: Journal of Structural Geology, v. 1, p. 299–307, doi: 10.1016/0191-8141(79)90004-X.

Fossen, H., and Tikoff, B., 1993, The deformation matrix for simultaneous simple shearing, pure shearing and volume change, and its application to transpression-transtension tectonics: Journal of Structural Geology, v. 15, p. 413–422, doi: 10.1016/0191-8141(93)90137-Y.

Fossen, H., Tikoff, B., and Teyssier, C., 1994, Strain modeling of transpression and transtensional deformation: Norsk Geologisk Tidsskrift, v. 74, p. 134–145.

Galehouse, J.S., 1967, Provenance and paleocurrents of the Paso Robles Formation, California: Geological Society of America Bulletin, v. 78, p. 951–978, doi: 10.1130/0016-7606(1967)78[951:PAPOTP]2.0.CO;2.

Gladwin, M.T., Gwyther, R.L., Hart, R.H.G., and Breckenridge, K.S., 1994, Measurements of the strain field associated with episodic creep events on the San Andreas fault at San Juan Bautista, California: Journal of Geophysical Research, v. 99, p. 4559–4565, doi: 10.1029/93JB02877.

Godfrey, N.J., Beaudoin, B.C., Klemperer, S.L., Levander, A.R., Luetgert, J.H., Meltzer, A.S., Mooney, W.D., and Trehu, A.M., 1997, Ophiolitic basement to the Great Valley forearc basin, California, from seismic and gravity data; implications for crustal growth at the North American continental margin: Geological Society of America Bulletin, v. 109, p. 1536–1562, doi: 10.1130/0016-7606(1997)109<1536:OBTTGV>2.3.CO;2.

Graham, R.H., 1978, Wrench faults, arcuate fold patterns and deformation in the southern French Alps: Proceedings of the Geologists' Association, v. 89, p. 125–142.

Graham, S.A., 1976, Tertiary stratigraphic and depositional environments near Indians Ranch, Monterey County, California, *in* Graham, S.A., ed., Tertiary and Quaternary geology of the Salinias Valley and Santa Lucia Range, Monterey County, California, Pacific Coast Paleogeography Field Guide 4: Society of Economic Paleontologists and Mineralogists, Pacific Section, v. 60, p. 3–12.

Graham, S.A., Stanley, R.G., Bent, J.V., and Carter, J.B., 1989, Oligocene and Miocene paleogeography of central California and displacement along the San Andreas fault: Geological Society of America Bulletin, v. 101, p. 711–730, doi: 10.1130/0016-7606(1989)101<0711:OAMPOC>2.3.CO;2.

Hackl, M., Malservisi, R., and Wdowinski, S., 2009, Strain rate patterns from dense GPS networks: Natural Hazards and Earth System Sciences, v. 9, p. 1177–1187, doi: 10.5194/nhess-9-1177-2009.

Hanson, K.L., Lettis, W.R., McLaren, M.K., Savage, W.U., and Hall, N.T., 2004, Style and Rate of Quaternary Deformation of the Hosgri Fault Zone, Offshore Southern California: U.S. Geological Survey Bulletin 1995-BB, 33 p.

Harbert, W., 1991, Late Neogene relative motions of the Pacific and North America plates: Tectonics, v. 10, p. 1–15, doi: 10.1029/90TC02093.

Hardebeck, J.L., Boatwright, J., Dreger, D., Goel, J., Graizer, V., Hudnut, K., Ji, C., Jones, L., Langbeing, J., Lin, E., Roeloffs, E., Simpson, R., Stark, K., Stein, R.S., and Tinsely, J.C., 2004, Preliminary report on the 22 December 2003 M6.5 San Simeon, California, earthquake: Seismological Research Letters, v. 75, p. 155–172, doi: 10.1785/gssrl.75.2.155.

Harding, T.P., 1976, Tectonic significance and hydrocarbon trapping consequences of sequential folding synchronous with San Andreas faulting, San Joaquin Valley, California: The American Association of Petroleum Geologists Bulletin, v. 60, p. 356–378.

Harding, T.P., 1988, State of stress near the San Andreas fault; implications for wrench tectonics; discussions: Geology, v. 16, p. 1151–1153, doi: 10.1130/0091-7613(1988)016<1151:COSOSN>2.3.CO;2.

Harris, R.A., and Segall, P., 1987, Detection of a locked zone at depth on the Parkfield, California, segment of the San Andreas fault: Journal of Geophysical Research, v. 92, p. 7945–7962, doi: 10.1029/JB092iB08p07945.

Hay, E.A., Hall, N.T., Cotton, W.R., Sylvester, A.G., and Crowell, J.C., 1989, Rapid creep on the San Andreas fault at Bitterwater, California, *in* Sylvester, A.G., and Crowell, J.C., eds., Sedimentation and Tectonics of Western North America: Volume 2. The San Andreas transform belt: Washington, D.C., American Geophysical Union, p. 36–39.

Heflin, M., Beriger, W., Blewitt, G., Freedman, A.P., Hurst, K., Lichten, S., Lindqwister, U.J., Vigue, Y., Webb, F., Yunck, T.P., and Zumberge, J., 1992, Global geodesy using GPS without fiducial sites: Geophysical Research Letters, v. 19, p. 131–134, doi: 10.1029/91GL02933.

Hill, M.L., and Dibblee, T.W., 1953, San Andreas, Garlock, and Big Pine faults, California: A study of the character, history, and tectonic significance of their displacements: Geological Society of America Bulletin, v. 64, p. 443–458, doi: 10.1130/0016-7606(1953)64[443:SAGABP]2.0.CO;2.

Jamison, W.R., 1987, Geometric analysis of fold development in overthrust terranes: Journal of Structural Geology, v. 9, p. 207–219, doi: 10.1016/0191-8141(87)90026-5.

Jamison, W.R., 1991, Kinematics of compressional fold development in convergent wrench terranes: Tectonophysics, v. 190, p. 209–232, doi: 10.1016/0040-1951(91)90431-Q.

Jennings, C.W., Strand, R.G., and Rogers, T.H., 1977, Geologic map of California: Sacramento, California, California Division of Mines and Geology, scale 1:750,000.

Johanson, I.A., and Burgmann, R., 2005, Creep and quakes on the northern transition zone of the San Andreas fault from GPS and InSAR data: Geophysical Research Letters, v. 32, p. L14306, doi: 10.1029/2005GL023150.

Johanson, I.A., Fielding, E.J., Rolandone, F., Buergmann, R., Harris, R.A., and Arrowsmith, J.R., 2006, Coseismic and postseismic slip of the 2004 Parkfield earthquake from space-geodetic data: Bulletin of the Seismological Society of America, v. 96, p. S269–S282, doi: 10.1785/0120050818.

Jones, R.R., Holdsworth, R.E., Clegg, P., McCaffrey, K., and Tavarnelli, E., 2004, Inclined transpression: Journal of Structural Geology, v. 26, p. 1531–1548, doi: 10.1016/j.jsg.2004.01.004.

King, C.Y., Nason, R.D., and Burford, R.O., 1977, Coseismic steps recorded on creep meters along the San Andreas fault: Journal of Geophysical Research, v. 82, p. 1655–1662, doi: 10.1029/JB082i011p01655.

King, N.E., Segall, P., and Prescott, W.H., 1987, Geodetic measurements near Parkfield, California, 1959–1984: Journal of Geophysical Research, v. 92, p. 2747–2766, doi: 10.1029/JB092iB03p02747.

Krantz, R.W., 1995, The transpressional strain model applied to strike-slip, oblique-convergent and oblique-divergent deformation: Journal of Structural Geology, v. 17, p. 1125–1137, doi: 10.1016/0191-8141(94)00129-N.

Lettis, W.R., 1985, Late Cenozoic stratigraphy and structure of the west margin of the central San Joaquin Valley, California, *in* Weide, D.L., and Faber, M.L., eds., Soils and Quaternary Geology of the Southwestern United States: Geological Society of America Special Paper, p. 97–114.

Lin, S., Jiang, D., and Williams, P.F., 1998, Transpression (or transtension) zones of triclinic symmetry; natural example and theoretical modelling: Geological Society of London Special Publication 135, p. 41–57, doi: 10.1144/GSL.SP.1998.135.01.04.

Lisowski, M., and Prescott, W.H., 1981, Short-range distance measurements along the San Andreas fault system in central California, 1975 to 1979: Bulletin of the Seismological Society of America, v. 71, p. 1607–1624.

Lisowski, M., Savage, J.C., and Prescott, W.H., 1991, The velocity field along the San Andreas fault in northern California: Journal of Geophysical Research, v. 96, p. 8369–8389, doi: 10.1029/91JB00199.

Mao, A., Harrison, G.A., and Dixon, T.H., 1999, Noise in GPS coordinate time series: Journal of Geophysical Research, v. 104, p. 2797–2816, doi: 10.1029/1998JB900033.

Márquez-Azúa, B., and DeMets, C., 2003, Crustal velocity field of Mexico from continuous GPS measurements, 1993 to June 2001; implications for the neotectonics of Mexico: Journal of Geophysical Research, v. 108, doi: 10.1029/2002JB002241.

Matthews, V., 1976, Correlation of Pinnacles and Neenach volcanic formations and their bearing on San Andreas fault problems: The American Association of Petroleum Geologists Bulletin, v. 60, p. 2128–2141.

Mavko, G.M., 1982, Fault interaction near Hollister, California: Journal of Geophysical Research, v. 87, p. 7807–7816, doi: 10.1029/JB087iB09p07807.

Mavko, G.M., Schulz, S.S., and Brown, B.D., 1985, Effects of the 1983 Coalinga, California, earthquake on creep along the San Andreas fault: Bulletin of the Seismological Society of America, v. 75, p. 475–489.

McKenzie, D., and Jackson, J., 1983, The relationship between strain rates, crustal thickening, palaeomagnetism, finite strain and fault movements within a deforming zone: Earth and Planetary Science Letters, v. 65, p. 182–202, doi: 10.1016/0012-821X(83)90198-X.

Medwedeff, D.A., 1989, Growth fault-bend folding at Southeast Lost Hills, San Joaquin Valley, California: The American Association of Petroleum Geologists Bulletin, v. 73, p. 54–67.

Menke, W., 1984, Geophysical Data Analysis; Discrete Inverse Theory: International Geophysics Series: New York, Academic Press, 289 p.

Miller, D.D., 1998, Distributed shear, rotation, and partitioned strain along the San Andreas fault, central California: Geology, v. 26, p. 867–870, doi: 10.1130/0091-7613(1998)026<0867:DSRAPS>2.3.CO;2.

Mitra, S., 2002, Structural models of faulted detachment folds: The American Association of Petroleum Geologists Bulletin, v. 86, p. 1673–1694.

Mitra, S., 2003, A unified kinematic model for the evolution of detachment folds: Journal of Structural Geology, v. 25, p. 1659–1673, doi: 10.1016/S0191-8141(02)00198-0.

Montgomery, D.R., 1993, Compressional uplift in the central California Coast Ranges: Geology, v. 21, p. 543–546, doi: 10.1130/0091-7613(1993)021<0543:CUITCC>2.3.CO;2.

Moore, D.E., and Rymer, M.J., 2007, Talc-bearing serpentinite and the creeping section of the San Andreas fault: Nature, v. 448, p. 795–797, doi: 10.1038/nature06064.

Mount, V.S., and Suppe, J., 1987, State of stress near the San Andreas fault; implications for wrench tectonics: Geology, v. 15, p. 1143–1146, doi: 10.1130/0091-7613(1987)15<1143:SOSNTS>2.0.CO;2.

Murray, J.R., Segall, P., Cervelli, P., Prescott, W.H., and Svarc, J.L., 2001, Inversion of GPS data for spatially variable slip-rate on the San Andreas fault near Parkfield, CA: Geophysical Research Letters, v. 28, p. 359–362, doi: 10.1029/2000GL011933.

Namson, J.S., and Davis, T.L., 1988, Seismically active fold and thrust belt in the San Joaquin Valley, central California: Geological Society of America Bulletin, v. 100, p. 257–273, doi: 10.1130/0016-7606(1988)100<0257:SAFATB>2.3.CO;2.

Nilsen, T.H., 1984, Offset along the San Andreas fault of Eocene strata from the San Juan Bautista area and

western San Emigdio Mountains, California: Geological Society of America Bulletin, v. 95, p. 599–609, doi: 10.1130/0016-7606(1984)95<599:OATSAF>2.0.CO;2.

Noriega, G.R., Arrowsmith, J.R., Grant, L.B., and Young, J.J., 2006, Stream channel offset and late Holocene slip rate of the San Andreas fault at the Van Matre Ranch Site, Carrizo Plain, California: Bulletin of the Seismological Society of America, v. 96, p. 33–47, doi: 10.1785/0120050094.

Odonne, F., and Vialon, P., 1983, Analogue models of folds above a wrench fault: Tectonophysics, v. 99, p. 31–46, doi: 10.1016/0040-1951(83)90168-3.

Okada, Y., 1985, Surface deformation due to shear and tensile faults in a half-space: Bulletin of the Seismological Society of America, v. 75, p. 1134–1154.

Page, B.M., 1970, Sur-Nacimiento fault zone of California: Continental margin tectonics: Geological Society of America Bulletin, v. 81, p. 667–690, doi: 10.1130/0016-7606(1970)81[667:SFZOCC]2.0.CO;2.

Page, B.M., 1981, The southern Coast Ranges, *in* Ernst, W.G., ed., The Geotectonic Development of California; Rubey Volume I: Englewood Cliffs, New Jersey, Prentice-Hall, p. 329–417.

Page, B.M., Thompson, G.A., and Coleman, R.G., 1998, Late Cenozoic tectonics of the central and southern Coast Ranges of California: Geological Society of America Bulletin, v. 110, p. 846–876, doi: 10.1130/0016-7606(1998)110<0846:OLCTOT>2.3.CO;2.

Pollitz, F.F., 1986, Pliocene change in Pacific plate motion: Nature, v. 320, p. 738–741, doi: 10.1038/320738a0.

Provost, A., Buisson, C., and Merle, O., 2004, From progressive to finite deformation and back: Journal of Geophysical Research, v. 109, doi: 10.1029/2001JB001734.

Ramsay, J.G., and Huber, M.I., 1983, The Techniques of Modern Structural Geology, Volume 1: Strain Analysis: London, Academic Press Limited, 307 p.

Rolandone, F., Bürgmann, R., Agnew, D.C., Johanson, I.A., Templeton, D.C., d'Alessio, M.A., Titus, S.J., DeMets, C., and Tikoff, B., 2008, Aseismic slip and fault-normal strain along the central creeping section of the San Andreas fault: Geophysical Research Letters, v. 35, p. L14305, doi: 10.1029/2008GL034437.

Rolandone, F., Bürgmann, R., Agnew, D.C., Johanson, I.A., Templeton, D.C., d'Alessio, M.A., Titus, S.J., DeMets, C., and Tikoff, B., 2009, Reply to comment by J.C. Savage on "Aseismic slip and fault-normal strain along the central creeping section of the San Andreas fault": Geophysical Research Letters, v. 36, p. L13306, doi: 10.1029/2009GL039167.

Ross, D.C., 1970, Quartz gabbro and anorthositic gabbro; markers of offset along the San Andreas fault in the California Coast Ranges: Geological Society of America Bulletin, v. 81, p. 3647–3661, doi: 10.1130/0016-7606(1970)81[3647:QGAAGM]2.0.CO;2.

Ryder, I., and Bürgmann, R., 2008, Spatial variations in slip deficit on the central San Andreas fault from InSAR: Geophysical Journal International, v. 175, p. 837–852, doi: 10.1111/j.1365-246X.2008.03938.x.

Sanderson, D.J., and Marchini, W.R.D., 1984, Transpression: Journal of Structural Geology, v. 6, p. 449–458, doi: 10.1016/0191-8141(84)90058-0.

Savage, J.C., 2009, Comment on "Aseismic slip and fault-normal strain along the central creeping section of the San Andreas fault": Geophysical Research Letters, v. 36, p. L13305, doi: 10.1029/2009GL037964.

Savage, J.C., and Burford, R.O., 1970, Accumulation of tectonic strain in California: Bulletin of the Seismological Society of America, v. 60, p. 1877–1896.

Savage, J.C., and Prescott, W.H., 1978, Asthenosphere readjustment and the earthquake cycle: Journal of Geophysical Research, v. 83, p. 3369–3376, doi: 10.1029/JB083iB07p03369.

Schmalzle, G., Dixon, T., Malservisi, R., and Govers, R., 2006, Strain accumulation across the Carrizo segment of San Andreas fault, California; impact of laterally varying crustal properties: Journal of Geophysical Research, v. 111, doi: 10.1029/2005JB003843.

Schulz, S.S., 1989, Catalog of Creepmeter Measurements in California from 1966 through 1988: U.S. Geological Survey Open File Report 89–0650, 193 p.

Schulz, S.S., Mavko, G.M., Burford, R.O., and Stuart, W.D., 1982, Long-term fault creep observations in central California: Journal of Geophysical Research, v. 87, p. 6977–6982, doi: 10.1029/JB087iB08p06977.

Shen, Z.-K., and Jackson, D.D., 1993, Global positioning system reoccupation of early triangulation sites; tectonic deformation of the southern Coast Ranges: Journal of Geophysical Research, v. 98, p. 9931–9946, doi: 10.1029/93JB00151.

Shen, Z.-K., Ge, B.X., Jackson, D.D., Potter, D., Cline, M., and Sung, L.-y., 1996, Northridge earthquake rupture models based on the global positioning system measurements: Bulletin of the Seismological Society of America, v. 86, p. 37–48.

Sieh, K.E., and Jahns, R.H., 1984, Holocene activity of the San Andreas fault at Wallace Creek, California: Geological Society of America Bulletin, v. 95, p. 883–896, doi: 10.1130/0016-7606(1984)95<883:HAOTSA>2.0.CO;2.

Simpson, G.D., Thompson, S.C., Noller, J.S., and Lettis, W.R., 1997, The northern San Gregorio fault zone; evidence for the timing of late Holocene earthquakes near Seal Cove, California: Bulletin of the Seismological Society of America, v. 87, p. 1158–1170.

Simpson, R.W., Schulz, S.S., Dietz, L.D., and Burford, R.O., 1988, The response of creeping parts of the San Andreas fault to earthquakes on nearby faults; two examples: Pure and Applied Geophysics, v. 126, p. 665–685, doi: 10.1007/BF00879014.

Sims, J.D., 1993, Chronology of displacement on the San Andreas fault in central California; evidence from reversed positions of exotic rock bodies near Parkfield, California: Geological Society of America Memoir 178, p. 231–256.

Stein, R.S., and Ekstrom, G., 1992, Seismicity and geometry of a 110-km-long blind thrust fault: 2. Synthesis of the 1982–1985 California earthquake sequence: Journal of Geophysical Research, v. 97, p. 4865–4883, doi: 10.1029/91JB02847.

Suppe, J., 1985, Principles of Structural Geology: Englewood Cliffs, New Jersey, Prentice Hall, 537 p.

Suppe, J., and Medwedeff, D.A., 1990, Geometry and kinematics of fault-propagation folding: Eclogae Geologicae Helvetiae, v. 83, p. 409–454.

Taliaferro, N.L., 1943, Geologic history and structure of the central Coast Ranges of California: California Division of Mines Bulletin, v. 118, p. 119–163.

Tetreault, J.L., 2006, Paleomagnetic, Structural, and Seismological Evidence for Oblique-Slip Deformation in Fault-Related Folds in the Rocky Mountain Foreland, Colorado Plateau, and Central Coast Ranges [Doctoral thesis]: Boulder, University of Colorado, 156 p.

Teyssier, C., and Tikoff, B., 1998, Strike-slip partitioned transpression of the San Andreas fault system; a lithospheric-scale approach: Geological Society of London Special Publication 135, p. 143–158, doi: 10.1144/GSL.SP.1998.135.01.10.

Tikoff, B., and Fossen, H., 1993, Simultaneous pure and simple shear; the unifying deformation matrix: Tectonophysics, v. 217, p. 267–283, doi: 10.1016/0040-1951(93)90010-H.

Tikoff, B., and Peterson, K., 1998, Physical experiments of transpression folding: Journal of Structural Geology, v. 20, p. 661–672, doi: 10.1016/S0191-8141(98)00004-2.

Titus, S.J., and Davis, J.R., 2009, Steady-state deformation using matrix exponentials: Eos (Transactions, American Geophysical Union), v. 90, no. 52, Fall Meeting supplement, abstract T33A–1871.

Titus, S.J., DeMets, C., and Tikoff, B., 2005, New slip rate estimates for the creeping segment of the San Andreas fault, California: Geology, v. 33, p. 205–208, doi: 10.1130/G21107.1.

Titus, S.J., DeMets, C., and Tikoff, B., 2006, Thirty-five-year creep rates for the creeping segment of the San Andreas fault and the effects of the 2004 Parkfield earthquake; constraints from alignment arrays, continuous global positioning system, and creepmeters: Bulletin of the Seismological Society of America, v. 96, p. S250–S268, doi: 10.1785/0120050811.

Titus, S.J., Housen, B., and Tikoff, B., 2007, A kinematic model for the Rinconada fault system in central California based on structural analysis of en echelon folds and paleomagnetism: Journal of Structural Geology, v. 29, p. 961–982, doi: 10.1016/j.jsg.2007.02.004.

Toppozada, T.R., Branum, D.M., Reichle, M.S., and Hallstrom, C.L., 2002, San Andreas fault zone, California: M≥5.5 earthquake history: Bulletin of the Seismological Society of America, v. 92, p. 2555–2601.

Toppozada, T.R., Branum, D.M., Harris, R.A., and Arrowsmith, J.R., 2006, San Andreas M approximately 6 earthquakes within 40 km of the Priest Valley end zone of the 1857 faulting: Bulletin of the Seismological Society of America, v. 96, p. S385–S396.

Townend, J., and Zoback, M.D., 2004, Regional tectonic stress near the San Andreas fault in central and southern California: Geophysical Research Letters, v. 31, doi: 10.1029/2003GL018918.

Treagus, J.E., and Treagus, S.H., 1981, Folds and the strain ellipsoid; a general model: Journal of Structural Geology, v. 3, p. 1–17, doi: 10.1016/0191-8141(81)90052-3.

Tsujimori, T., Liou, J.G., and Coleman, R.G., 2007, Finding of high-grade tectonic blocks from the New Idria serpentinite body, Diablo Range, California; petrologic constraints on the tectonic evolution of an active serpentinite diapir, *in* Cloos, M., Carlson, W.D., Gilbert, M.C., Liou, J.G., and Sorensen, S.S., eds., Convergent margin terranes and associated regions: A tribute to W.G. Ernst: Geological Society of America Special Paper 419, p. 67–80.

Wentworth, C.M., and Zoback, M.D., 1989, The style of late Cenozoic deformation at the eastern front of the California Coastal Ranges: Tectonics, v. 8, p. 237–246, doi: 10.1029/TC008i002p00237.

Working Group on California Earthquake Probabilities (WGCEP), 2002, Earthquake Probabilities in the San Francisco Bay Region: U.S. Geological Survey Open-File Report 03-214, 235 p.

White, R., 1987, Paleomagnetism of the Tulare Formation from Cores and Surface Exposures, West-Central and Southwestern San Joaquin Valley [Master's thesis]: Long Beach, California State University, 272 p.

Wickham, J., 1995, Fault displacement-gradient folds and the structure at Lost Hills, California (U.S.A.): Journal of Structural Geology, v. 17, p. 1293–1302, doi: 10.1016/0191-8141(95)00029-D.

Wilcox, R.E., Harding, T.P., and Seely, D.R., 1973, Basic Wrench Tectonics: The American Association of Petroleum Geologists Bulletin, v. 57, p. 74–96.

Wilkinson, E.R., 1960, Vallecitos field: California Oil Fields Summary Operations, v. 45, p. 17–33.

Wojtal, S.F., 1989, Measuring displacement gradients and strains in faulted rocks: Journal of Structural Geology, v. 11, p. 669–678, doi: 10.1016/0191-8141(89)90003-5.

Woodring, W.P., Stewart, R.B., and Richards, R.W., 1940, Geology of the Kettleman Hills Oil Field, California; Stratigraphy, Paleontology, and Structure: U.S. Geological Survey Professional Paper 195, 170 p.

Zoback, M.D., Zoback, M.L., Mount, V.S., Suppe, J., Eaton, J.P., Healy, J.H., Oppenheimer, D.H., Reasenberg, P.A., Jones, L.M., Raleigh, C.B., Wong, I.G., Scotti, O., and Wentworth, C.M., 1987, New evidence on the state of stress of the San Andreas fault system: Science, v. 238, p. 1105–1111, doi: 10.1126/science.238.4830.1105.

Zumberge, J.F., Heflin, M.B., Jefferson, D.C., Watkins, M.M., and Webb, F.H., 1997, Precise point positioning for the efficient and robust analysis of GPS data from large networks: Journal of Geophysical Research, v. 102, p. 5005–5017, doi: 10.1029/96JB03860.

Manuscript Received 10 August 2009
Revised Manuscript Received 23 March 2010
Manuscript Accepted 12 May 2010

Printed in the USA